GSA Data Repository 2019249

Kremer, C.H., Mustard, J.F., and Bramble, M.S., 2019, A widespread olivine-rich ash deposit on Mars: Geology, https://doi.org/10.1130/G45563.1

SUPPLEMENTARY MATERIAL

ITEM DR1. DATA AND METHODS

DR1.1. Mapping

Our mapping of the outcrop extent of the circum-Isidis olivine-rich unit (Figs. DR1-3) was guided at the regional scale using previously published spectroscopic maps of the distribution of olivine enrichments (Hamilton and Christensen, 2005; Tornabene et al., 2008) based on data from the Thermal Emission Imaging System for the Mars 2001 Odyssey mission (Christensen et al., 2004) and the Mars Global Surveyor Thermal Emission Spectrometer experiment (Christensen et al., 2001). Regional-scale mapping was also guided by multispectral reduced data record mapping tiles (Seelos et al., 2017) from the Compact Reconnaissance Imaging Spectrometer for Mars (CRISM) (Murchie et al., 2007). At the 1:50,000 scale, our mapping was guided by geomorphic features observed in orbital imagery from the High Resolution Imaging Science Experiment (HiRISE) (McEwen et al., 2007) (Table DR1) and imagery mosaics (Dickson et al., 2018) from the Context Camera (CTX) (Malin et al., 2007). We identified the unit based on geomorphic criteria considered to be uniquely diagnostic of the unit within the regional stratigraphy. In HiRISE imagery, these characteristics include fracturing and banding (Bramble et al,. 2017). In CTX imagery, diagnostic characteristics include corrugated texture, banding in some exposures, and “mottled” tonality, which is equivalent to the fracturing observed in higher-resolution HiRISE imagery (Goudge et al., 2015). The olivine-rich unit's overall light tonality is visible in both HiRISE and CTX imagery (Goudge et al., 2015; Bramble et al., 2017). Geomorphic mapping was also guided by the interpreted stratigraphic position of the unit, namely, observations of the unit overlying the massive regional basement unit and underlying the pitted mafic capping unit. The unit's superposition by local outcrops of layered sulfate-rich rocks and ~3.6 Ga lavas (Ehlmann and Mustard, 2012; Bramble et al., 2017) was also used to guide mapping in small locales within the Northeast Syrtis area. Geomorphic mapping at the 1:50,000 scale was validated using spectral summary parameters for olivine from CRISM Targeted Reduced Data Records (Murchie et al., 2007) (Table DR2). Mapping in the Jezero watershed (Goudge et al., 2015), the Northeast Syrtis region (Bramble et al., 2017), and the Libya Montes region (Tornabene et al., 2008) was adapted and modified from previous mapping efforts at various scales. We have not included in our map spectral detections of olivine in the ejecta of impact craters that have penetrated Isidis Planitia, which Tornabene et al. (2008) interpreted as having exhumed the olivine-rich unit from depth.

Mapping of the inferred extent of the olivine-rich unit in the dust-covered northern Nili Fossae plains was based on thermal infrared spectral mapping by Hamilton and Christensen (2005) and on diagnostic morphologies observed in orbital imagery, which are discussed further in the caption to Figure DR3. The results of our mapping at the regional scale were overlaid on a mosaic of CTX imagery (see Fig. 1A).

DR1.2. Outcrop Orientation, Thickness, and Extent

We used the NASA Ames Stereo pipeline (Broxton and Edwards, 2008; Moratto et al., 2010; Shean et al., 2016) to create digital elevation models (DEMs) containing olivine-rich unit outcrops for assessing the unit's thickness, stratigraphy, banding orientation, and topographic distribution (Table DR3). DEMs from HiRISE stereo pairs and CTX imagery were tied to Mars

Orbiter Laser Altimeter (MOLA) (Smith et al., 2001) shot points, and MOLA elevation data and DEMs from the High Resolution Stereo Camera (HRSC) (Neukum and Jaumann, 2004) were also used for assessing the unit's topographic distribution. We used grid resolutions of ≤1 m for HiRISE and ~21 m for CTX (McEwen et al., 2007; Malin et al., 2007). The vertical precisions of HiRISE, CTX, and HRSC DEMs are at least ~0.50 m, ≤10 m, and ~40 m, respectively (Neukum and Jaumann, 2004; McEwen et al., 2007; Fergason et al., 2017).

We made a total of ~700 thickness measurements for ~120 outcrops by measuring the total elevation change between the topographically highest and lowest exposures of the unit (Table DR4). We prioritized measuring thicknesses of exposures of the olivine-rich unit where *both* top and bottom contacts with the mafic capping unit and basement unit, respectively, were observed (Fig. DR4). It is likely that exposures of the olivine-rich unit without observed top unit-contacts have experienced erosion, meaning that thickness measurements of these exposures without top contacts likely underestimate the unit's original thickness. Similarly, wherever we measure exposures of the unit where no lower contact with the basement unit is observed, we also underestimate the thickness of the olivine-rich unit because we do not know how deep below the subsurface the contact lies. Meanwhile, as noted in the main text, parallelism between the olivine-rich unit's bedding and its top-contact with the overlying mafic capping unit suggests that the olivine-rich unit was likely not heavily eroded before emplacement of the capping unit. This suggests that the thickness of olivine-rich unit, wherever it is exposed with both its top and bottom unit contacts, likely represents the unit's original, non-eroded thickness. We note in our plots and tables which exposures of the unit do not exhibit both top and bottom contacts (and therefore constitute underestimates of thickness) and which exposures of the unit exhibit both top and bottom contacts. We measured only cliff- or mesa-forming stratigraphic sections that outcropped over a limited distance (~<1 km) to avoid measuring large-scale undulations in the topography of the underlying basement unit.

We find that the olivine-rich unit's average thickness in Nili Fossae is on the order of ~10 m (Fig. 4). Previous studies overestimated (e.g., Ehlmann and Mustard, 2012; Edwards and Ehlmann, 2015) the average thickness of the unit through a combination of: 1) using lower resolution topographic data (e.g., MOLA) and 2) measuring topography as a proxy for the unit's thickness where no unit contacts were exposed (and thereby likely measuring undulations in the basement unit draped by the olivine-rich unit).

We estimated the orientations of banding in the olivine-rich and of the unit's top and bottom stratigraphic contacts by extracting elevations from DEMs and fitting a plane to the non-collinear point cloud for each band or contact (Table DR5). We measured dips only for outcrops where non-collinear point clouds could be extracted from well-exposed, continuous beds or unit contacts. After measuring the apparent thickness of each outcrop using the Spatial Analyst tool in ArcMap, we corrected the apparent thicknesses of non-flat-lying outcrops to true thickness using the measured dip of banding, which we interpreted as layering. We compared estimated dips from our plane-fitting work to dips estimated from visual inspection of the topographic trends of 'stair-step' tabular bedding observed in cross section (Fig. DR5) as an additional test on the quality of our fits.

We do not specify a strict threshold for similarity in orientation values in order for layers or contacts in a given locale to qualify as parallel. Given the highly undulose nature of the basement unit's topography, even a rock unit that mantles this topography and has parallel internal layering should exhibit somewhat variable structural orientations over the geographic extent of a given outcrop. Because the basement-defined topography in Libya Montes is more rugged than in Nili Fossae and because the bedding orientations of the olivine-rich unit in Libya Montes vary more as a result, one would expect conformable beds in Libya Montes to exhibit a wider range of dips as measured in orbital data than in Nili Fossae. As discussed in the results section of the main text (see Fig. 3), each outcrop in Libya Montes generally exhibits a wider range of dips than in Nili Fossae.

The hypothesized emplacement scenarios imply different thicknesses of layering within the olivine-rich unit, and so we estimated average band thickness per outcrop by dividing the thicknesses of each outcrop by the numbers of bands observed per outcrop. It was possible to observe bands whose thickness values are below the pixel resolution of HiRISE imagery because the horizontal expressions of these bands are above the resolution of HiRISE, especially where the unit outcrops on broad, shallowly dipping slopes. In Nili Fossae we tabulated the thicknesses of olivine-rich unit bands only on complete stratigraphic sections but also noted thin banding in incomplete stratigraphic sections (see Fig. DR6).

We estimated the area of exposure for the unit in the Nili Fossae (~43,000 km^2) and Libya Montes (~1700 km^2) regions, as well as its inferred extent in the northern Nili Fossae region (28,000 km^2) using the Spatial Analyst Toolbox in ArcMap. Distal pyroclasts should cover a wide elevation range, and we therefore extracted the elevations covered by the unit from Mars Orbiter Laser Altimeter (MOLA) data (Smith et al., 2001).

ITEM DR2. SUPPLEMENTARY DATA FOR UNIT ORIGINS

We provide supplementary data for constraining the origin of the circum-Isidis olivine-rich unit. While all of the evidence that is essential to constraining the olivine-rich unit's origin is presented in the main text, this supplementary material provides, for the sake of thoroughness, several supporting and ancillary pieces of evidence, which agree with the pyroclastic origin of the olivine-rich unit. A summary of these data is given in Table DR6.

DR2.1. Circum-Isidis Distribution

One of the notable observations of the olivine-rich unit is its circumferential distribution relative to Isidis Planitia. This circumferential distribution in part motivated previous interpretations that the olivine-rich unit originated as an impact melt sheet from the Isidis-forming impact (e.g., Mustard et al., 2009). As we find in the main text, however, the unit could not have originated as impact products from Isidis, and so its distribution circumferential to Isidis Planitia is likely circumstantial. We also note here that the layered and friable olivine-rich unit of the greater circum-Isidis region strongly differs morphologically, stratigraphically, and texturally from the evidently indurated and geomorphically massive olivine-rich rocks of the greater circum-Argyre and circum-Hellas regions (for overview, see Ehlmann and Edwards, 2014), consistent with the inference that the circum-Isidis olivine-rich unit's circumferential distribution is a coincidence.

In the Nili Fossae region, the unit is bordered to the east and south by younger volcanic units (Hiesinger and Head, 2004). Indeed, the ejecta of impact craters penetrating Isidis Planitia contain spectrally detected enrichments of olivine, suggesting that the olivine-rich unit may be present beneath Isidis Planitia (Tornabene et al., 2008). The unit in the Nili Fossae region is bordered to the west and north by dust-covered terrain, where spectral and morphological evidence for the unit would be obscured. In the Libya Montes region, the unit is bordered to the north by younger volcanic units and to the south by terrain that has been heavily dissected by valley networks (Bishop et al., 2013). The friable nature of the olivine-rich unit (Rogers et al., 2018) would facilitate its denudation from regions with extensive histories of impact cratering or overland water flow. For these reasons, it is plausible that an ancient pyroclastic deposit could exhibit an apparently circum-Isidis distribution on modern Mars.

DR2.2. Topographic Expression: Crater Superposition

As noted in the main text, the minimum elevation of the olivine-rich unit above the surrounding terrain interior or exterior to Jezero crater and to the three unnamed crater-like structures (at 21.9°N, 78.2°E; 22.5°N, 79.1°E; and 22.7°N, 79.4°E, respectively) far exceeds the olivine-rich unit's maximum non-eroded thickness. We also note that, in addition to not being observed in the present study, rim-piercing dikes are rare in most craters (Pilkington and Grieve, 1992). At Hashir crater in Libya Montes, lavas that in-filled from outside the crater are unlikely to account for the unit's superposition of the crater's lower inner-rim above the unit's contact with the capping unit, as the crater rim rises 100s of meters above the terrain exterior to the crater (Fig. DR 9). These observations provide additional support for the argument that the olivine-rich unit did not emplace as lava flows.

DR2.3. Unit Stratigraphy

DR2.3.1. Planar Bedding and Sand Sheets

Ubiquitous absence of resolvable cross stratification (Fig. DR6) could hypothetically be accounted for by deposition of the olivine-rich unit as part of a vast sand sheet, which would have had planar bedding (Livingstone and Warren, 1996). However, sand sheets on Earth have never been observed to persist over regions of nearly 10^5 km^2 or to span ~4,000 m of elevation change and rarely produce deposits more than several meters thick (Livingstone and Warren, 1996). Moreover, sand sheets are typically observed to be proximal to much larger non-sheet-forming sand seas. Collectively, these observations of the olivine-rich unit and terrestrial sand sheets further rule out a sand sheet-related erg origin of the olivine-rich unit.

DR2.3.2. Komatiite Bedding Thicknesses and Continuity

Terrestrial komatiites commonly exhibit approximately meter-scale or thicker bedding (Arndt, 1986; Nisbet et al., 1987). Although decimeter- to centimeter-scale layering is observed sporadically in terrestrial komatiites, such thin flow-units commonly occur inter-bedded with significantly thicker flows, and even these locally thin flow-units may vary in thickness significantly along strike in visible pinch-and-swell structures (Arndt, 1986). Moreover, bedding in komatiites, especially for bed thicknesses at the decimeter- or centimeter-scale, is typically highly discontinuous over kilometer-scale exposures (Arndt, 1986). This contrasts markedly with the continuously layered exposures of the olivine-rich unit over distances of up to several kilometers (Fig. DR6). Observations of the thicknesses of terrestrial komatiites agree with evidence against a lava-flow origin for the olivine-rich unit.

DR2.4. Grain Size and Composition from Spectroscopy

DR2.4.1. Erg Grain Size and Composition

The interpretation of 1 mm grains in the olivine-rich unit from Hapke modeling of single-scattering albedo derived from CRISM data (Edwards and Ehlmann, 2015) gives a substantially larger grain size than has been measured for most windblown sediment on Mars. In orbital datasets, the interpreted grain sizes of non-lithfied wind-blown sand deposits on Mars range from 100 µm to 1 mm with an average of 500 µm (Edgett and Christensen, 1991). Grain sizes measured *in situ* for non-lithified wind-blown sand deposits by the Opportunity rover at Eagle crater, by the Spirit rover at El Dorado, and by the Curiosity rover at the Namib Dune and Bagnold Dune Field are ~50-150 µm (Soderblom et al., 2004), ~200-300 µm (Sullivan et al., 2005), ~200-300 µm, and ~50-500 µm (Lapotre et al., 2016), respectively. Grain sizes of 1 mm are observed *in situ* in non-lithified, isolated, and volumetrically limited coarse-grained ripple crests (Jerolmack et al., 2006), and isolated inactive bedforms at Gale crater have been measured to have average grain sizes of <500 µm (Weitz et al., 2018). Lithified deposits of wind-blown sand range from 300 µm and 1.0 mm at Meridiani Planum (Squyres et al., 2004) and 62.5 µm to 1.0 mm at Gale Crater (Sacks et al., 2017).

Moreover, despite the observation of sand seas on Mars today (e.g., Lancaster and Greeley, 1990) and evidence that hydrodynamic sorting may increase the concentration of relatively mechanically stable olivine in martian aeolian sands (Fedo et al., 2015), there is presently no observation of erg deposits with areal extents of ~10^4-10^5 km^2 that have concentrated sediment derived from olivine-bearing mafic basalts to apparently picrite-like compositions (Rogers et al., 2018). Altogether, the spectroscopically inferred grain size and composition remain problematic for hypotheses about aeolian epiclastic origins for the highly areally extensive olivine-rich unit of the circum-Isidis region.

DR2.4.2. Ash Grain Size and Composition

As mentioned in the main text, the spectrally inferred composition and grain size of the olivine-rich unit resemble those of crystal-rich, coarse-grained clastic rocks observed *in situ* at Columbia Hills, which are interpreted by consensus (Francis, 2011) to be pyroclastic deposits. We briefly synthesize the characteristics of the two classes of ash-fall deposits from Columbia Hills. Crystal-rich (~40% Fo_{72-75} olivine), coarse-grained (~1 mm), olivine-rich pyroclasts are interpreted to comprise the Comanche class rock unit in Columbia Hills (McCoy et al., 2008; Morris et al., 2010). Rocks of similar crystallinity, grain size, and composition also occur as part of the Algonquin class rock unit (Ruff et al., 2014), and pyroclasts of mafic composition and a high degree of cyrstallinity (~55% crystalline) have also been interpreted to constitute the rock units at the Home Plate outcrop in Columbia Hills (Squyres et al., 2007; Lewis et al., 2008; Ming et al., 2008; Yingst et al., 2010).

REFERENCES CITED

Arndt, N., 1986, Differentiation of komatiite flows: Journal of Petrology, v. 27, p. 279–301, doi:10.1093/petrology/27.2.279.

Bramble, M.S., Mustard, J.F., and Salvatore, M.R., 2017, The geological history of Northeast Syrtis Major, Mars: Icarus, v. 293, p. 66–93, doi:10.1016/j.icarus.2017.03.030.

Broxton, M.J., and Edwards, L.J., 2008, The Ames Stereo Pipeline: Automated 3D surface reconstruction from orbital imagery: Houston, Texas, Lunar and Planetary Institute, Lunar and Planetary Science XXXIX, abstract 2419.

Christensen, P.R. et al., 2001, Mars Global Surveyor Thermal Emission Spectrometer experiment: investigation description and surface science results: Journal of Geophysical Research, v. 106, p. 23,823-871.

Christensen, P.R., Jakosky, B.M., Kiefer, H.H., Malin, M.C., McSween, H.Y., Mehall, G.L., Silverman, S., Ferry, S., Caplinger, M.A., and Ravine, M.A., 2004, The Thermal Emission Imaging System (THEMIS) for the Mars 2001 Odyssey Mission: Space Science Reviews, v. 110, p. 85–130.

Dickson, J.L., Kerber, L., Fassett, C.I., and Ehlmann, B.L., 2018, A Global, Blended CTX Mosaic of Mars with Vectorized Seam Mapping: A New Mosaicking Pipeline Using Principles of Non-Destructive Image Editing: Houston, Texas, Lunar and Planetary Institute, Lunar and Planetary Science XLIX, abstract 2840.

Edgett, K.S., and Christensen, P.R., 1991, The particle size of martian aeolian dunes: Journal of Geophysical Research, v. 96, p. 22765–22776, doi:10.1029/91JE02412.

Edwards, C.S., and Ehlmann, B.L., 2015, Carbon sequestration on Mars: Geology, v. 43, p. 863–866, doi:10.1130/G36983.1.

Ehlmann, B.L., and Mustard, J.F., 2012, An in-situ record of major environmental transitions on early Mars at Northeast Syrtis Major: Geophysical Research Letters, v. 39, p. L11202, doi:10.1029/2012GL051594.

Fedo, C.M., McGlynn, I.O., and McSween, H.Y., 2015, Grain size and hydrodynamic sorting controls on the composition of basaltic sediments: Implications for interpreting martian soils: Earth and Planetary Science Letters, v. 423, p. 67–77, doi:10.1016/j.epsl.2015.03.052.

Fergason, R.L., Kirk, R.L., and Cushing, G., 2017, Analysis of local slopes at the InSight landing site on Mars: Space Science Reviews, v. 211, p. 109–133, doi:10.1007/s11214-016-0292-x.

Francis, D., 2011, Columbia Hills — An exhumed layered igneous intrusion on Mars? Earth and Planetary Science Letters, v. 310, p. 59–64, doi:10.1016/j.epsl.2011.08.003.

Goudge, T.A., Mustard, J.F., Head, J.W., Fassett, C.I., and Wiseman, S.M., 2015, Assessing the mineralogy of the watershed and fan deposits of the Jezero crater paleolake system, Mars: Jezero Paleolake System Mineralogy: Journal of Geophysical Research: Planets, v. 120, p. 775–808, doi:10.1002/2014JE004782.

Hamilton, V.E., and Christensen, P.R., 2005, Evidence for extensive, olivine-rich bedrock on Mars: Geology, v. 33, p. 433–436, doi:10.1130/G21258.1.

Jerolmack, D.J., Mohrig, D., Grotzinger, J.P., Fike, D.A., and Watters, W.A., 2006, Spatial grain size sorting in eolian ripples and estimation of wind conditions on planetary surfaces: Application to Meridiani Planum, Mars: Journal of Geophysical Research: Planets, v. 111, p. E12S02, doi:10.1029/2005JE002544.

Keszthelyi, L., McEwen, A.S., and Thordarson, T., 2000, Terrestrial analogs and thermal models for Martian flood lavas: Journal of Geophysical Research: Planets, v. 105, p. 15027–15049, doi:10.1029/1999JE001191.

Lancaster, N., and Greeley, R., 1990, Sediment volume in the north polar sand seas of Mars: Journal of Geophysical Research, v. 95, p. 10921, doi:10.1029/JB095iB07p10921.

Lapotre, M.G.A. et al., 2016, Large wind ripples on Mars: A record of atmospheric evolution: Science, v. 353, p. 55–58, doi:10.1126/science.aaf3206.

Lewis, K.W., Aharonson, O., Grotzinger, J.P., Squyres, S.W., Bell, J.F., Crumpler, L.S., and Schmidt, M.E., 2008, Structure and stratigraphy of Home Plate from the Spirit Mars Exploration Rover: Journal of Geophysical Research, v. 113, doi:10.1029/2007JE003025.

Livingstone, I., and Warren, A., 1996, Aeolian Geomorphology: An Introduction: Harlow, Addison Wesley Longman, 211 p.

Malin, M.C. et al., 2007, Context Camera Investigation on board the Mars Reconnaissance Orbiter: Journal of Geophysical Research, v. 112, doi:10.1029/2006JE002808.

McCoy, T.J. et al., 2008, Structure, stratigraphy, and origin of Husband Hill, Columbia Hills, Gusev Crater, Mars: Journal of Geophysical Research, v. 113, doi:10.1029/2007JE003041.

McEwen, A.S. et al., 2007, Mars Reconnaissance Orbiter's High Resolution Imaging Science Experiment (HiRISE): Journal of Geophysical Research: Planets, v. 112, p. E05S02, doi:10.1029/2005JE002605.

McSween, H.Y. et al., 2008, Mineralogy of volcanic rocks in Gusev Crater, Mars: Reconciling Mössbauer, Alpha Particle X-Ray Spectrometer, and Miniature Thermal Emission Spectrometer spectra: Journal of Geophysical Research, v. 113, p. E06S04, doi:10.1029/2007JE002970.

Ming, D.W. et al., 2008, Geochemical properties of rocks and soils in Gusev Crater, Mars: Results of the Alpha Particle X-Ray Spectrometer from Cumberland Ridge to Home Plate: Journal of Geophysical Research, v. 113, p. E12S39, doi:10.1029/2008JE003195.

Moratto, Z.M., Broxton, M.J., Beyer, R.A., Lundy, M., and Husmann, K., 2010, Ames Stereo Pipeline, NASA’s open source automated stereogrammetry software: Houston, Texas, Lunar and Planetary Institute, Lunar and Planetary Science XLI, abstract 2364.

Morris, R.V. et al., 2010, Identification of Carbonate-Rich Outcrops on Mars by the Spirit Rover: Science, v. 329, p. 421–424, doi:10.1126/science.1189667.

Murchie, S. et al., 2007, Compact Reconnaissance Imaging Spectrometer for Mars (CRISM) on Mars Reconnaissance Orbiter (MRO): Journal of Geophysical Research, v. 112, p. E05S03, doi:10.1029/2006JE002682.

Mustard, J.F., Ehlmann, B.L., Murchie, S.L., Poulet, F., Mangold, N., Head, J.W., Bibring, J.-P., and Roach, L.H., 2009, Composition, Morphology, and Stratigraphy of Noachian Crust around the Isidis basin: Journal of Geophysical Research, v. 114, doi:10.1029/2009JE003349.

Neukum, G., and Jaumann, R., 2004, HRSC: The high resolution stereo camera of Mars Express: Mars Express: The Scientific Payload, p. 17–35.

Nisbet, E.G. et al., 1987, Uniquely fresh 2.7 Ga komatiites from the Belingwe greenstone belt, Zimbabwe: Geology, v. 15, p. 1147–1150, doi:10.1130/0091-7613(1987)15<1147:UFGKFT>2.0.CO;2.

Pilkington, M., and Grieve, R.A.F., 1992, The geophysical signature of terrestrial impact craters: Reviews of Geophysics, v. 30, p. 161–181, doi:10.1029/92RG00192.

Ruff, S.W., Niles, P.B., Alfano, F., and Clarke, A.B., 2014, Evidence for a Noachian-aged ephemeral lake in Gusev crater, Mars: Geology, v. 42, p. 359–362, doi:10.1130/G35508.1.

Sacks, L.E., Edgar, L.A., Edwards, C.S., and Anderson, R.B., 2017, Grain scale analyses of the Murray and Stimson formations using data from the Mars Science Laboratory Mars Hand Lens Imager and the Chemcam remote micro imager: Houston, Texas, Lunar and Planetary Institute, Lunar and Planetary Science XLVIII, abstract 2595.

Seelos, F.P., Romeo, G., Hash, C.D., and Garhart, E.C., 2017, CRISM multispectral and hyperspectral mapping data - observing modes, accumulated coverage, data products, and tile mosaics: Houston, Texas, Lunar and Planetary Institute, Lunar and Planetary Science XLVIII, abstract 7113.

Shean, D.E., Alexandrov, O., Moratto, Z.M., Smith, B.E., Joughin, I.R., Porter, C., and Morin, P., 2016, An automated, open-source pipeline for mass production of digital elevation models (DEMs) from very-high-resolution commercial stereo satellite imagery: ISPRS

Journal of Photogrammetry and Remote Sensing, v. 116, p. 101–117, doi:10.1016/j.isprsjprs.2016.03.012.

Smith, D.E. et al., 2001, Mars Orbiter Laser Altimeter: Experiment summary after the first year of global mapping of Mars: Journal of Geophysical Research: Planets, v. 106, p. 23689–23722, doi:10.1029/2000JE001364.

Soderblom, L.A. et al., 2004, Soils of Eagle Crater and Meridiani Planum at the Opportunity Rover Landing Site: Science, v. 306, p. 1723–1726, doi:10.1126/science.1105127.

Squyres, S.W. et al., 2004, In Situ Evidence for an Ancient Aqueous Environment at Meridiani Planum, Mars: Science, v. 306, p. 1709–1714, doi:10.1126/science.1104559.

Squyres, S.W. et al., 2007, Pyroclastic activity at home plate in Gusev Crater, Mars: Science, v. 316, p. 738–742, doi:10.1126/science.1139045.

Sullivan, R. et al., 2005, Aeolian processes at the Mars Exploration Rover Meridiani Planum landing site: Nature, v. 436, p. 58–61, doi:10.1038/nature03641.

Tornabene, L.L., Moersch, J.E., McSween, H.Y., Hamilton, V.E., Piatek, J.L., and Christensen, P.R., 2008, Surface and crater-exposed lithologic units of the Isidis Basin as mapped by coanalysis of THEMIS and TES derived data products: Journal of Geophysical Research, v. 113, doi:10.1029/2007JE002988.

Weitz, C.M., Sullivan, R.J., Lapotre, M.G.A., Rowland, S.K., Grant, J.A., Baker, M., and Yingst, R.A., 2018, Sand Grain Sizes and Shapes in Eolian Bedforms at Gale Crater, Mars: Geophysical Research Letters, v. 45, p. 9471–9479, doi:10.1029/2018GL078972.

Yingst, R.A., Crumpler, L., Farrand, W.H., Li, R., and de Souza, P., 2010, Constraints on the geologic history of “Home Plate” materials provided by clast morphology and texture: Journal of Geophysical Research, v. 115, p. E00F13, doi:10.1029/2010JE003668.

Supplementary Figures

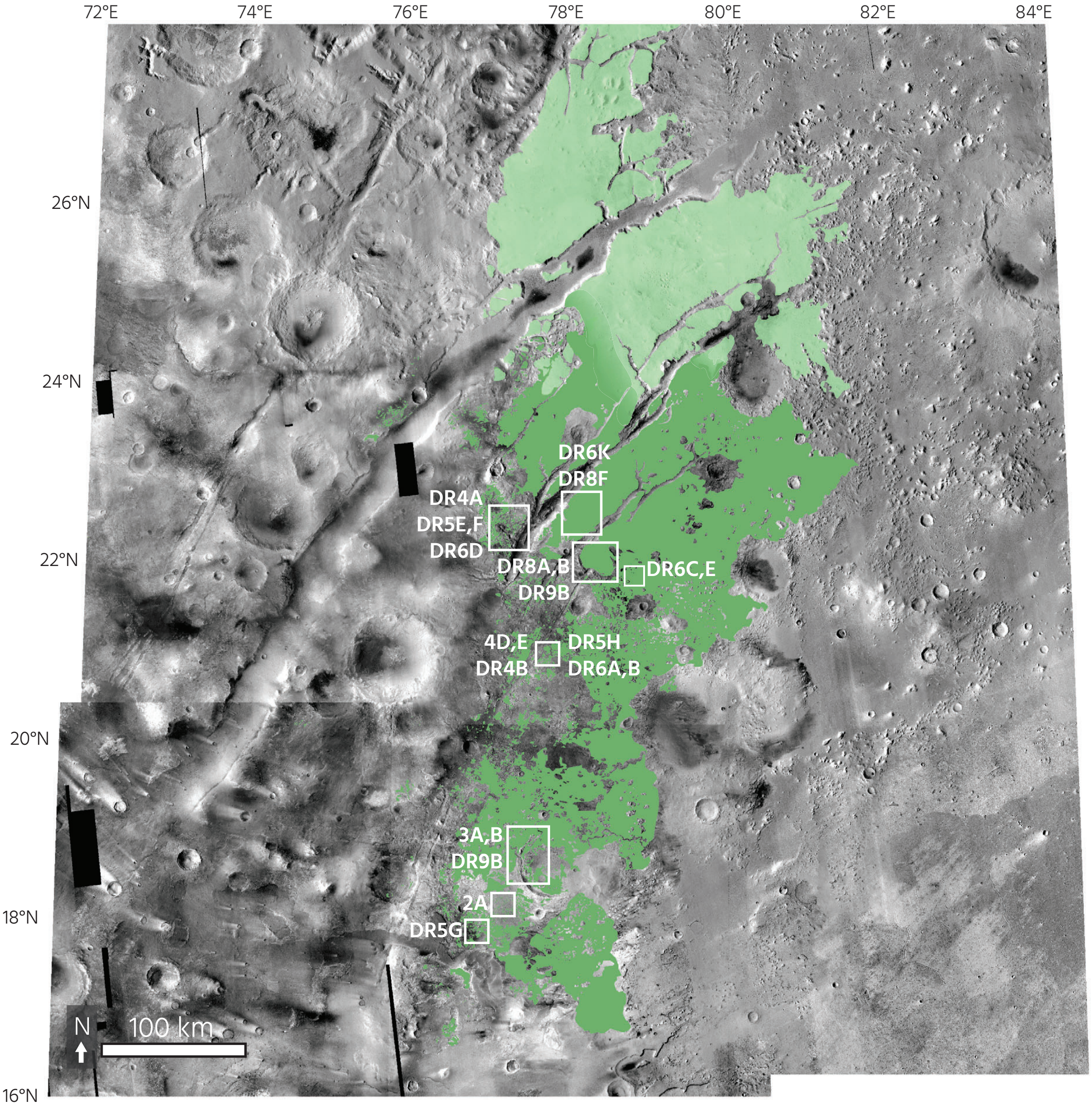

Figure DR1. Distribution of the circum-Isidis olivine-rich unit (green) in the Nili Fossae region mapped at the 1:50,000 scale. In addition to criteria discussed in the methodology section, our regional-scale mapping was informed in part by THEMIS spectral mapping by Hamilton and Christensen (2005). Our mapping was adapted in part and modified from geomorphic mapping by Bramble et al. (2017) in Northeast Syrtis (17°N-18°N, 76°E-78°E) at the 1:1000 scale and Goudge et al. (2015) in the Jezero watershed (18°N-21°N, 75°E-79°E) at the 1:100,000 scale. Mapping was subsequently overlaid on a blended mosaic of CTX imagery (Dickson et al., 2018). The inferred extent of the olivine-rich unit in the dust-covered northern Nili Fossae region is indicated in light green. The methodology of mapping this gradational contact between the olivine-rich unit and its inferred extent is given in the text of the Data Repository (see also Fig. DR3). This map is a higher-resolution equivalent of **Figure 1B** in the main text. The approximate locations of figures in the main text and the Data Repository are shown here with white boxes. See imagery IDs in appropriate captions for precise locations of imagery.

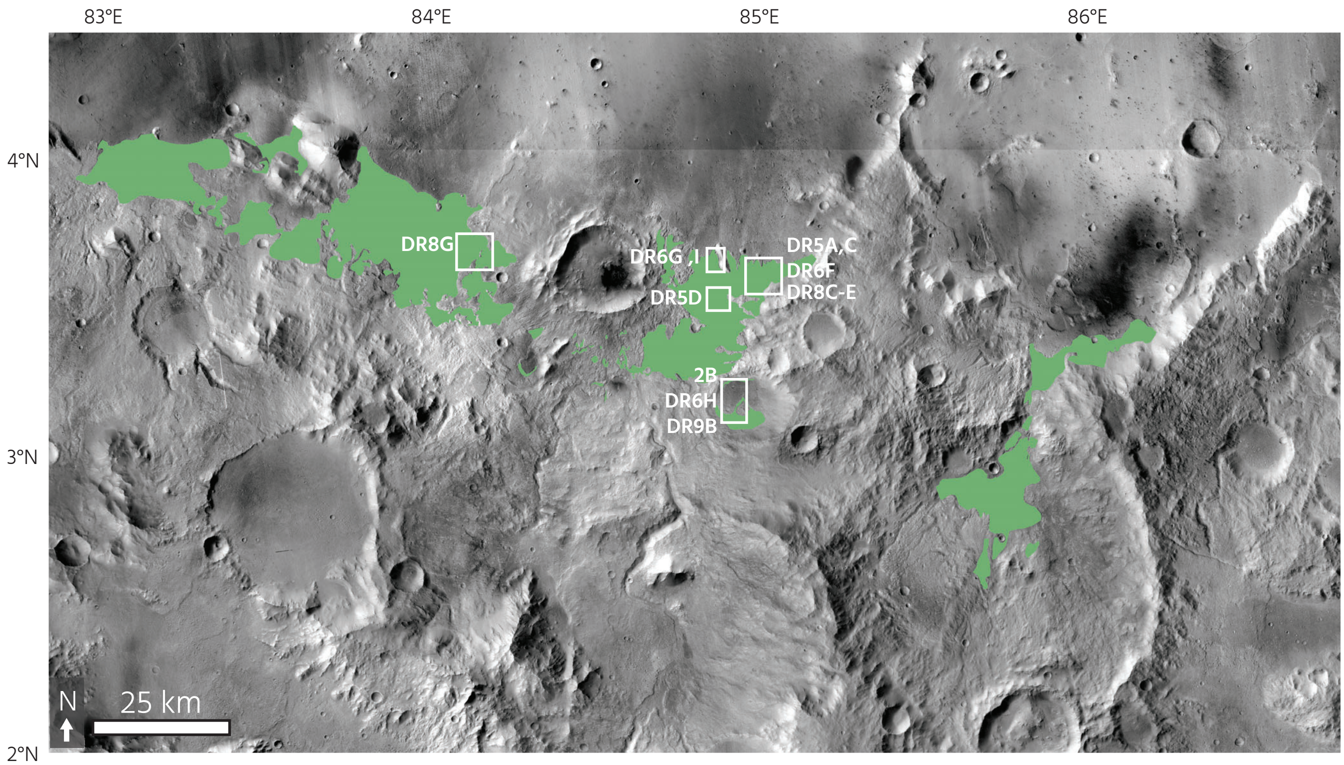

Figure DR2. Distribution of the circum-Isidis olivine-rich unit (green) in the Libya Montes region. Mapped geomorphically at the 1:50,000 scale, adapted in part from lower-scale TES- and THEMIS-based spectral mapping by Tornabene et al. (2008). This figure is the equivalent of **Figure 1C** in the main text.

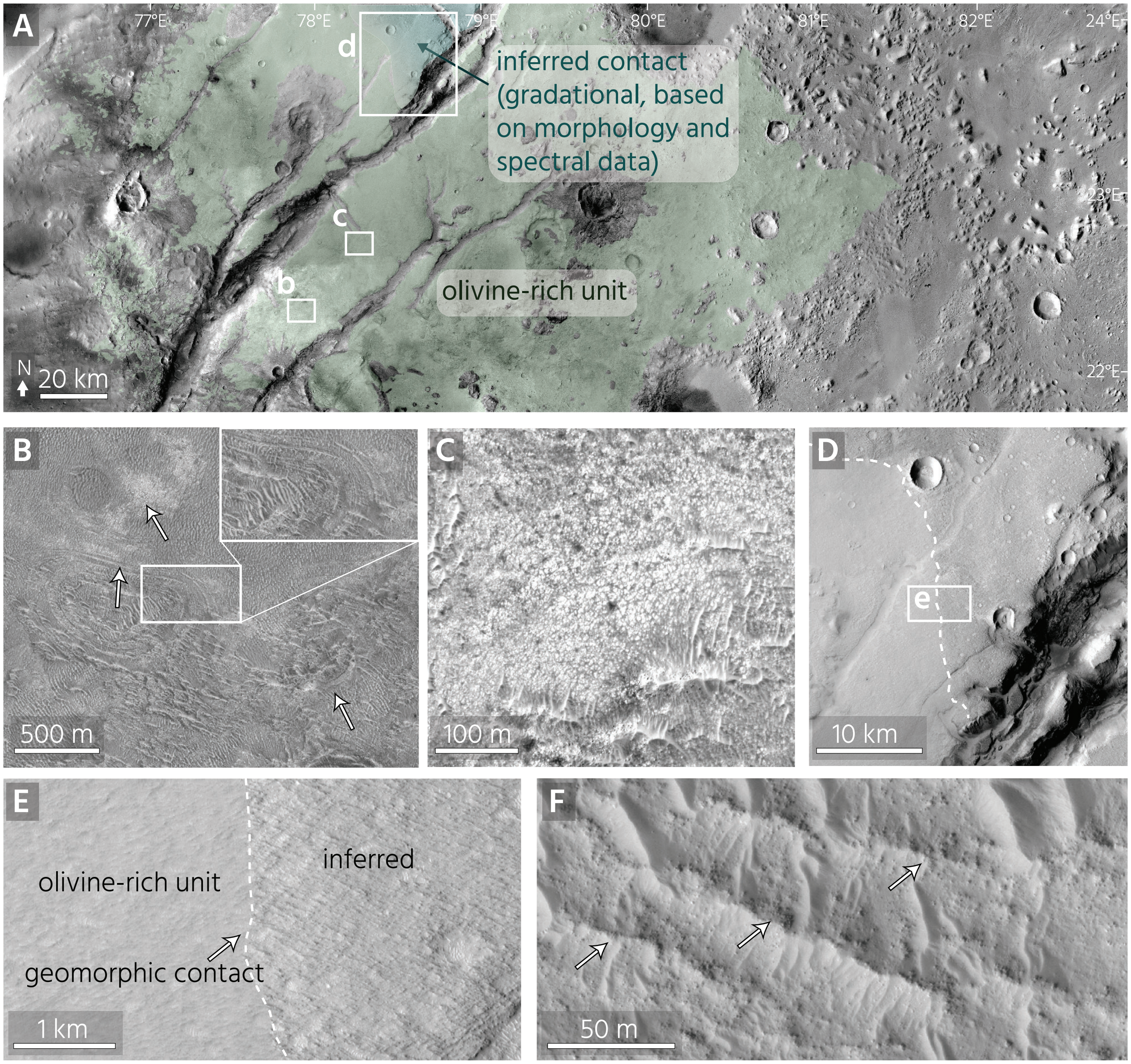

Figure DR3. Mapping methodology for the circum-Isidis olivine-rich unit in the dust-mantled northern Nili Fossae region. (A) Map of the olivine unit in Nili Fossae, showing its relatively gradational contact with the areas in northern Nili Fossae where the unit is inferred to occur (indicated in light blue here, for graphical contrast). The gradational contact between the olivine-rich unit proper and its inferred northernmost extent has been extended by several degrees of latitude to the north relative to spectral mapping by Hamilton and Christensen et al. (2005), based on the appearance of diagnostic morphologies in orbital imagery.

(B) Banding and meter-scale polygonal fracturing (HiRISE image ESP_026570_2025) exposed in region where unit has light tonality in CTX. (C) Locally exposed light-tonality and meter-scale polygonal fracturing where the unit is regionally dust-mantled (HiRISE image ESP_035352_2025). (D) Geomorphic contact between the morphologically smooth regions where there is morphological evidence for the olivine-rich unit and the rough, "corrugated" regions where the unit is inferred to occur under the extensively dust-mantled northern Nili Fossae plains. The geomorphic contact is more distinctive than the spectrally inferred contact (Hamilton and Christensen, 2005). Presence of the unit is inferred in northern Nili Fossae based on spectral mapping by Hamilton and Christensen (2005) and the lack of abrupt topographic discontinuity at the contact between rock exposures with light tonality, polygonal fracturing, and banding (olivine-rich unit) and rock exposures with corrugated surface and poor crater retention (heavily eroded capping unit). (E) The corrugated surface visible in CTX mosaic in the northern Nili Fossae region shows strong morphological similarity to exposures of the unit elsewhere in the greater Isidis Planitia region that bear yardangs or yardang-like morphologies. (F) Elongate parallel ridges in northern Nili Fossae, such as the ones that comprise the corrugated surface shown in E are visible in HiRISE imagery (ESP_029247_2045). They are evidently bedrock ridges and not dunes because they shed boulder-sized debris (arrows). Streamlined ridges in bedrock such as yardangs typically develop in friable rocks (e.g., Ward, 1979), whose presence in the northern Nili Fossae region, together with the foregoing features observed in orbital imagery, suggest that the olivine-rich unit is present in these dust-mantled regions.

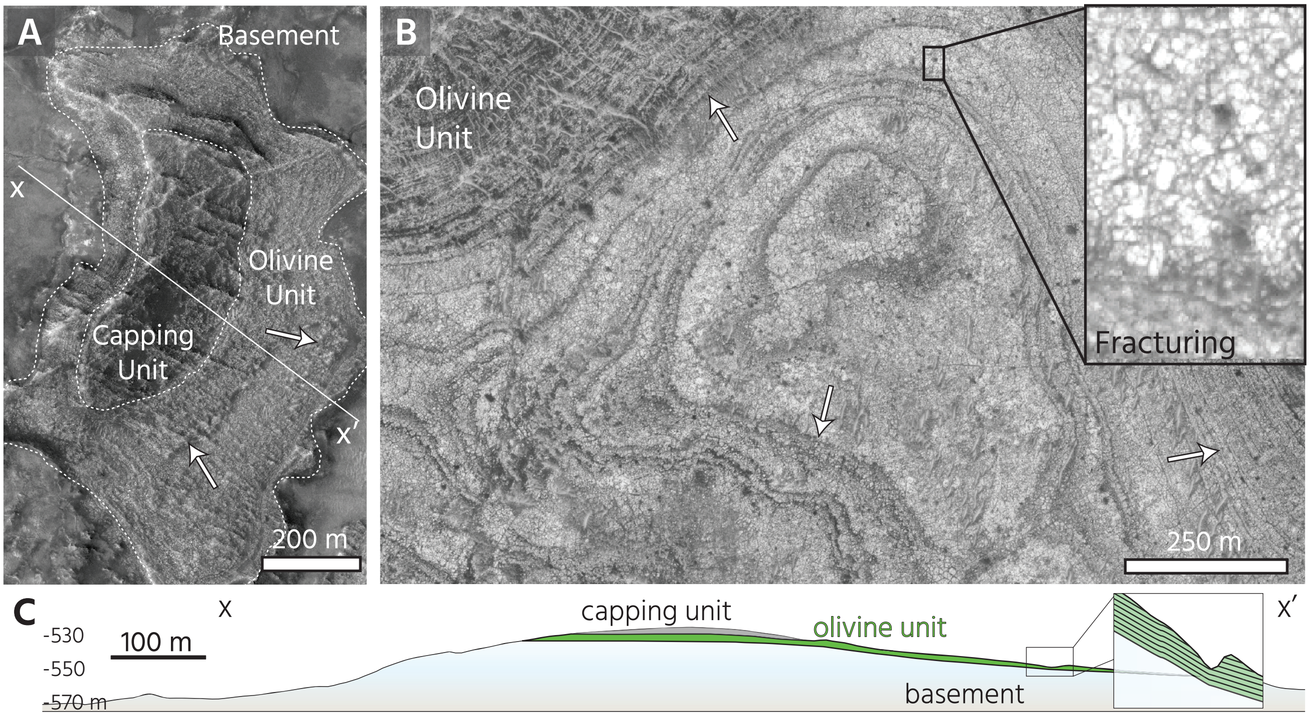

Figure DR4. Stratigraphy and morphology of the olivine-rich unit as shown in two representative exposures in Nili Fossae. (A) Stratigraphy of olivine-rich unit, capping unit, and basement unit (HiRISE image PSP_005855_2020) with layering highlighted by arrows. (B) Overall light tonality, banding with locally alternating tonality (arrows), and fracturing (inset) characteristic of the olivine-rich unit, in a different locality in Nili Fossae (HiRISE image ESP_044662_2010). (C) Interpreted cross section of olivine-rich unit in regional stratigraphy for outcrop in (A) using topography from CTX images F05_037607_2008_XN_20N282W and F05_037752_2008_XN_20N282W. Inset shows draping of topography by banding. Bands whose thicknesses are near or below the maximum HiRISE resolution of ~25 cm/pixel are identifiable because they outcrop over broad expanses of gently sloping terrain. Inset vertical exaggeration ~10x.

Figure DR5. Representative examples of geomorphic expressions of draping of basement topography by the olivine-rich unit and of conformability between the olivine-rich unit and the mafic capping unit (see **Figure 2**) Arrows (white in DEMs, black in cross sections) indicate "stair-step" and/or tabular bedding visible in topographic profiles. Locations of lines of section are shown draped on DEMs in white, with same L-R orientation. Cross section insets show zoomed versions of interpreted cross-sections and have been vertically exaggerated relative to cross sections to highlight stair-step or tabular topographic expression of bedding (black arrows). Elevations from DEMs are given to the left on each cross section in meters.

(A) Parallel and continuous layers of the olivine-rich drape a local bulge in the basement (HiRISE DEM DTEEC_016034_1835_017089_1835_A01).

(B) Approximately flat-lying layers of the olivine-rich unit overlain conformably by the capping unit on flat basement outcrop (HiRISE DEM DTEEC_016443_1980_015942_1980_U01). DEM inset shows stair-step bedding in DEM data. Equivalent to **Figure 2A**. **2B** uses HiRISE DTEEC_002756_1830_002822_1830_A01

(C and D) Parallel and continuous layers of the olivine-rich unit drape a local bulge in the basement (C: HiRISE DEM DTEEC_016034_ 1835_017089_1835_A01, D: DEM from HiRISE stereopair ESP_042763_183 ESP_ 043264_1835). Tabular bedding shown in inset in D.

(E, F and G) Draping of topographic lows by the olivine-rich unit and the capping unit. (E: DEM from HiRISE stereopair ESP_ 027691_2025 and ESP_ 026992_2025 F: HiRISE DEM DTEEC_ 002888_2025_ 002176_202 5_A01, G: DEM from HiRISE stereopair ESP_ 024513_1980 and ESP_025 370_1980).

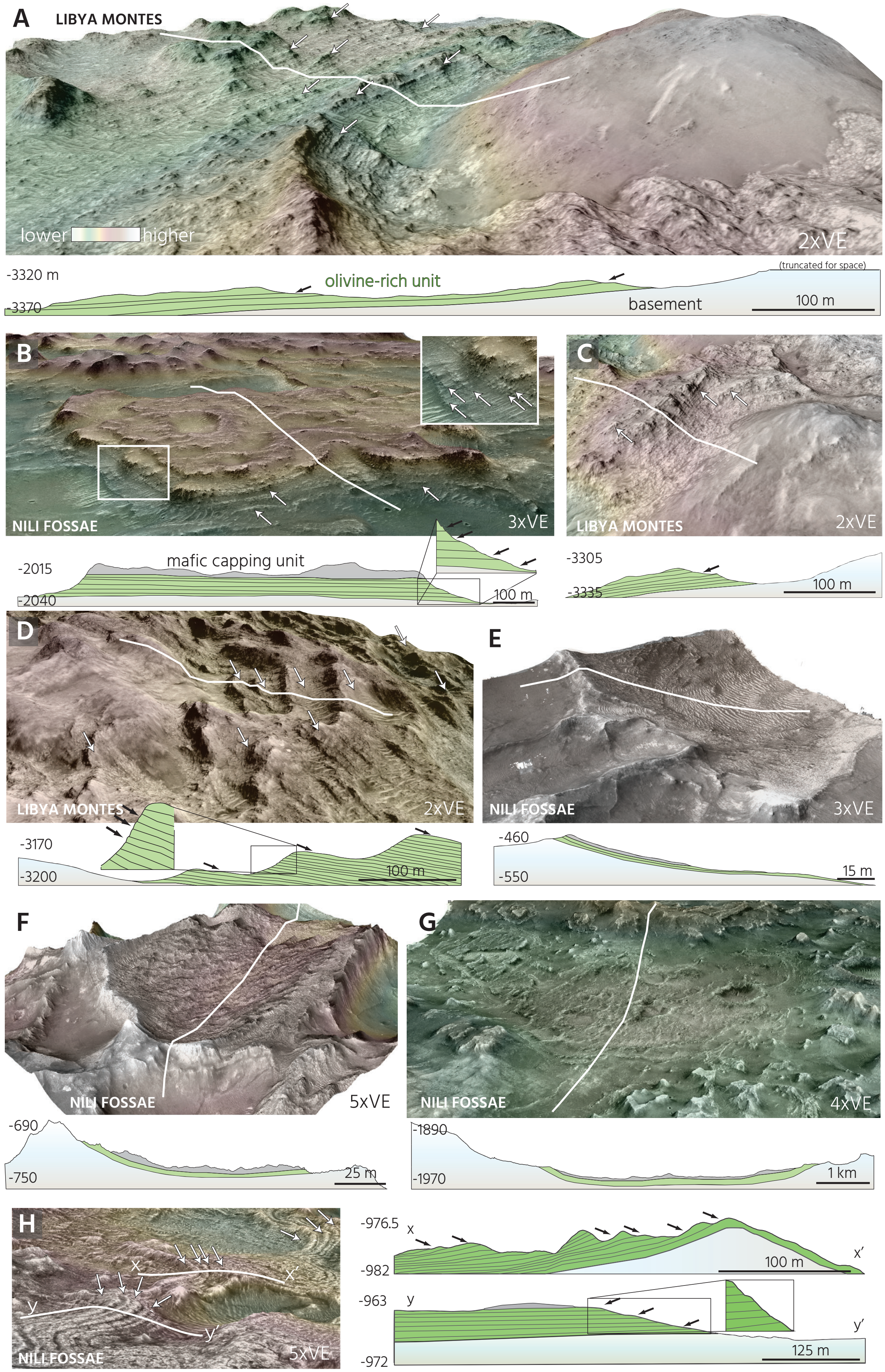

(H) Example of typically well-bedded olivine-rich unit in Nili Fossae (DEM from HiRISE stereopair ESP_044 095_2010 and ESP_044 662_2010). Equivalent geographic area to that shown in **Figure 4D,E** in the main text, but here viewed looking south.

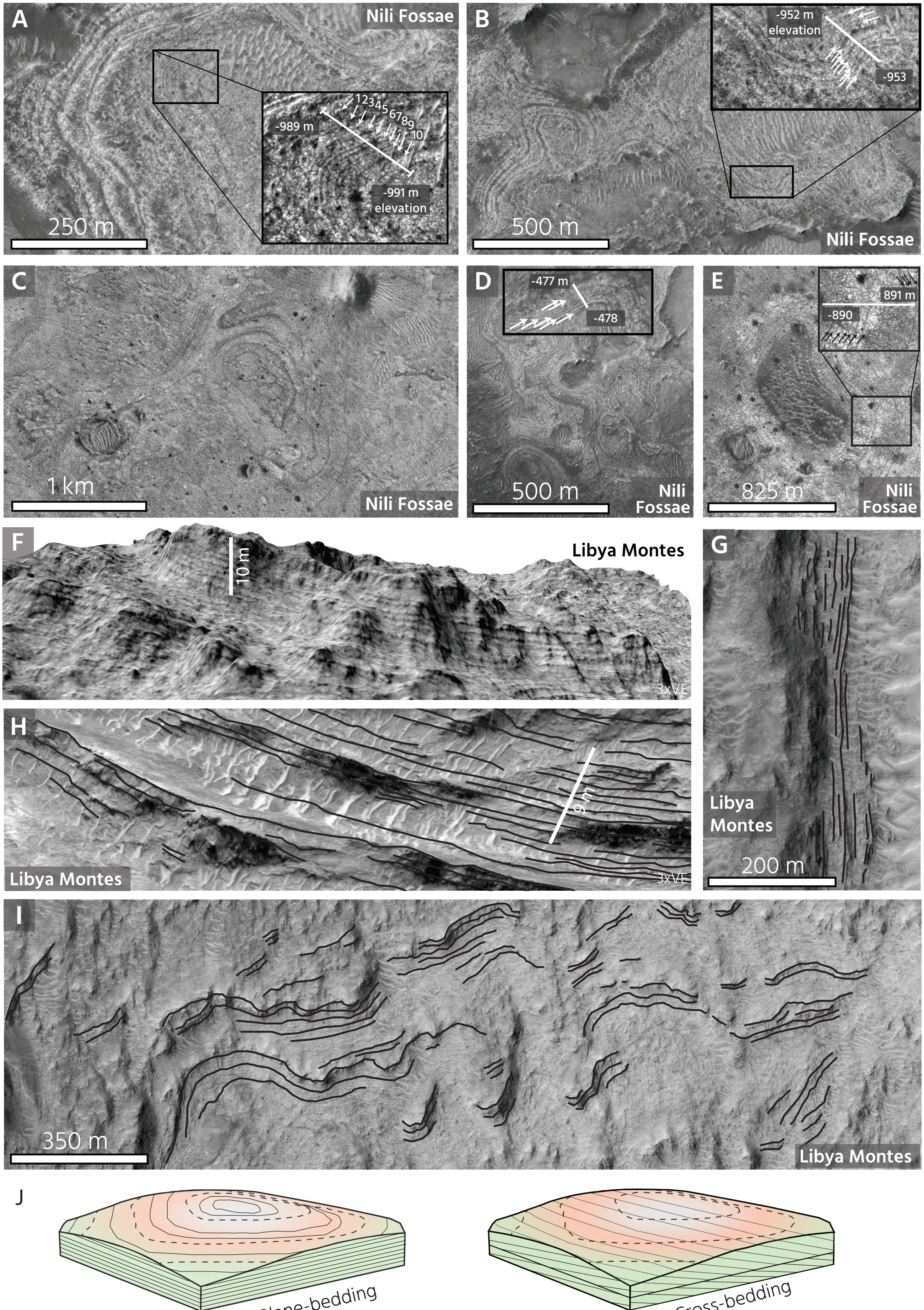

Fig. DR6. See next page for caption.

Fig. DR6 (cont.) Compare the above imagery with plane-bedding shown in Figure 2 in the main text and in the following figure. (J) Block diagrams illustrating plan-view and cross-sectional expression of plane-bedding and cross-bedding. Dashed lines give topographic contours.

(This Page) (K) Example of continuous banding observed in the olivine-rich unit. The entire section of banding is exposed over ~3.4 km, with the longest continuously resolvable banding in this section spanning ~3.1 km. (L) Zoomed-in version of the previous panel, showing parallel banding (highlighted in white) in a 450 m long segment of the banding. The most extensively continuously exposed band noted in the previous panel is highlighted in green. Many individual bands visible in this figure are continuous over at least 1 km (HiRISE image ESP_026570_2025).

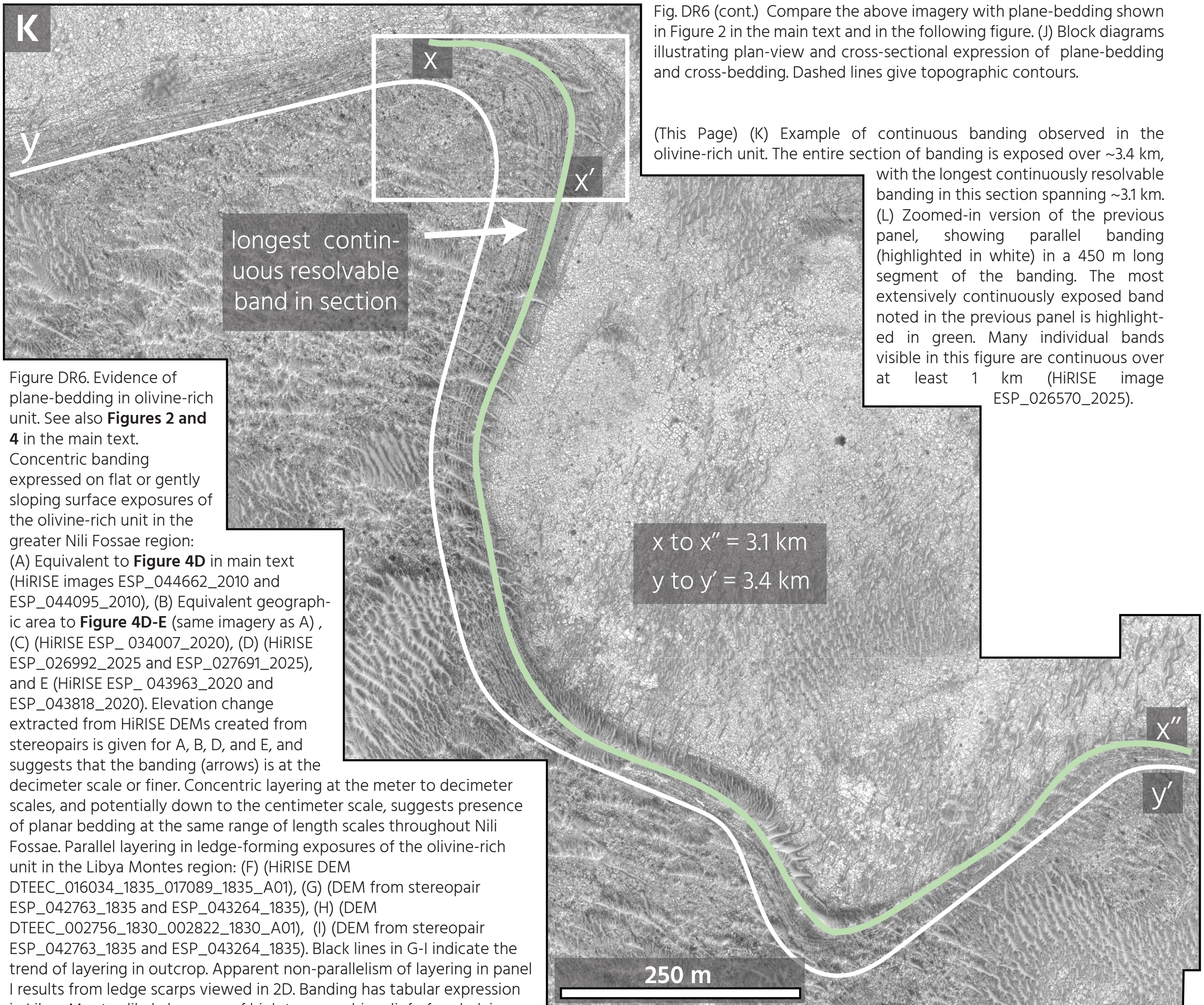

Figure DR6. Evidence of plane-bedding in olivine-rich unit. See also **Figures 2 and 4** in the main text. Concentric banding expressed on flat or gently sloping surface exposures of the olivine-rich unit in the greater Nili Fossae region: (A) Equivalent to **Figure 4D** in main text (HiRISE images ESP_044662_2010 and ESP_044095_2010), (B) Equivalent geographic area to **Figure 4D-E** (same imagery as A) , (C) (HiRISE ESP_ 034007_2020), (D) (HiRISE ESP_026992_2025 and ESP_027691_2025), and E (HiRISE ESP_ 043963_2020 and ESP_043818_2020). Elevation change extracted from HiRISE DEMs created from stereopairs is given for A, B, D, and E, and suggests that the banding (arrows) is at the decimeter scale or finer. Concentric layering at the meter to decimeter scales, and potentially down to the centimeter scale, suggests presence of planar bedding at the same range of length scales throughout Nili Fossae. Parallel layering in ledge-forming exposures of the olivine-rich unit in the Libya Montes region: (F) (HiRISE DEM DTEEC_016034_1835_017089_1835_A01), (G) (DEM from stereopair ESP_042763_1835 and ESP_043264_1835), (H) (DEM DTEEC_002756_1830_002822_1830_A01), (I) (DEM from stereopair ESP_042763_1835 and ESP_043264_1835). Black lines in G-I indicate the trend of layering in outcrop. Apparent non-parallelism of layering in panel I results from ledge scarps viewed in 2D. Banding has tabular expression in Libya Montes likely because of high topographic relief of underlying basement. For tabular expression of olivine-rich unit in Nili Fossae, see Figures 2, 5, and DR5.

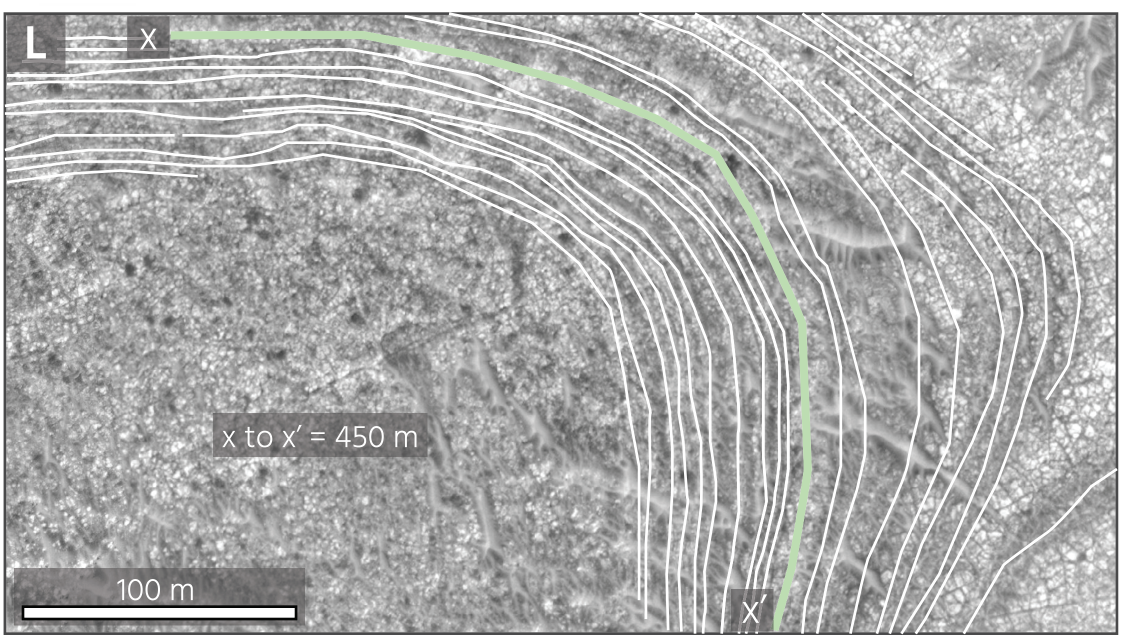

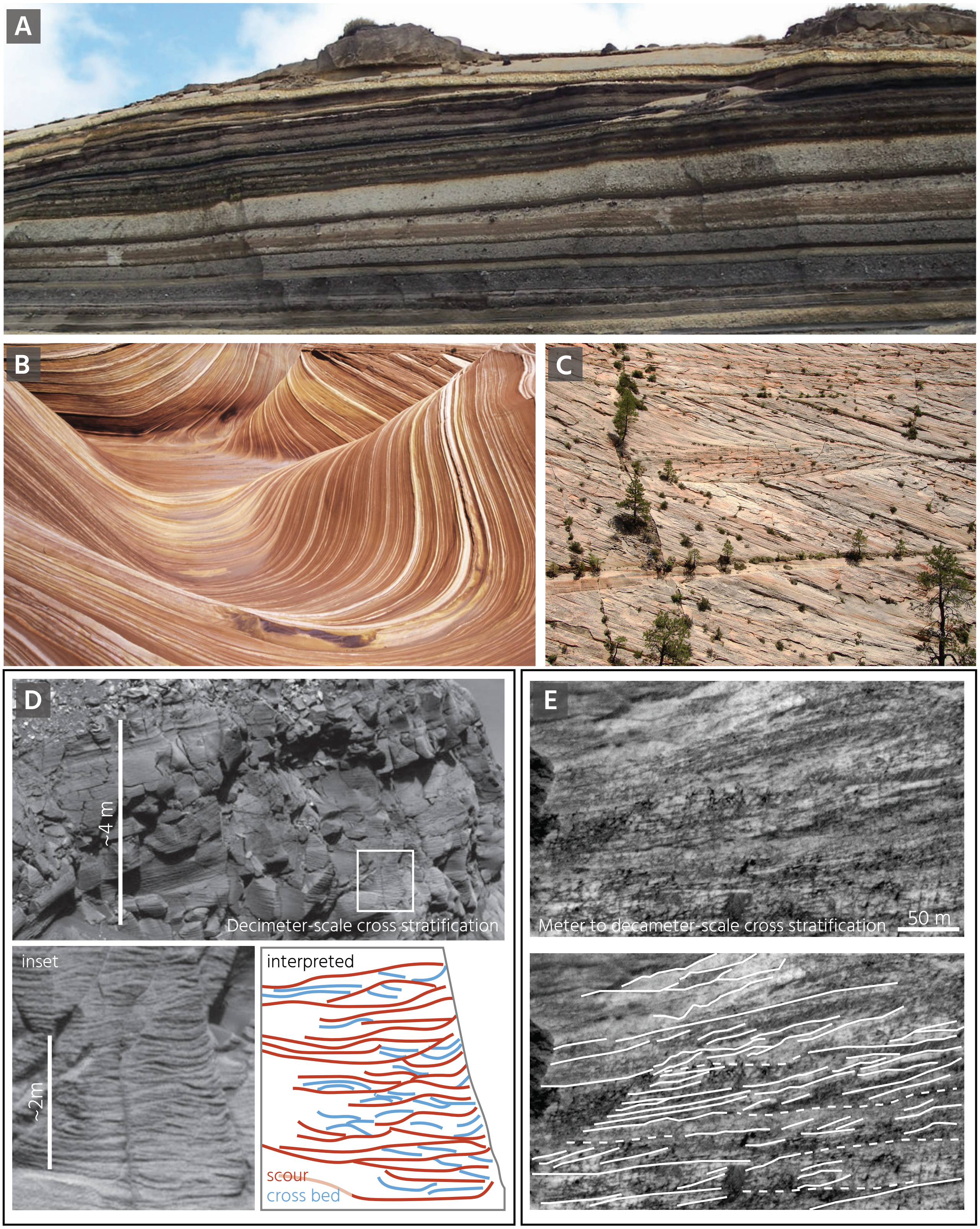

Figure DR7. **Examples of plane-bedding and cross-bedding in terrestrial clastic deposits as possible analogs for the circum-Isidis olivine-rich unit.** (A) Plane-bedded ash-fall deposits of the Andean volcano Chimborazo in ~5 m thick outcrop. Cross-bedded aeolian sandstone in Arizona in (B) ~10 m tall and (C) 30 m thick outcrops. Plane-bedding in volcanic ash is shown in cross section, and cross-bedding shown in aeolian sandstone shown in plan view (B) and cross-sectional view (B and C). Compare these field photographs with block diagrams in Figure DR6. The plane-bedding shown above resembles the bedding observed in the olivine-rich unit at the meter- to decimeter-scales, and potentially locally down to the centimeter scale (see Figure 5 in the main text and the previous figure). Alternating dark and light banding in terrestrial ash-fall deposits provides potential analog for the alternating light and dark banding in the olivine-rich unit. All Earth images used under Creative Commons license.

Aeolian clastic deposits on Mars. (D) Decimeter-scale bedding in eolian deposits of the Cape St. Mary outcrop, Victoria Crater (MER Pancam image P2441, sol 1212) with interpretations of bedding structures (after Lapotre et al., 2016). (E) Meter to decameter-scale cross stratification in Mt. Sharp at Gale Crater (ESP_012551_1750) with interpretations of bedding structures (after Milliken et al., 2014). These styles of discontinuous and non-parallel internal stratification contrast with the styles of continuous and parallel bedding at the decameter to decimeter-scales, and likely down to the centimeter-scale of layer thickness.

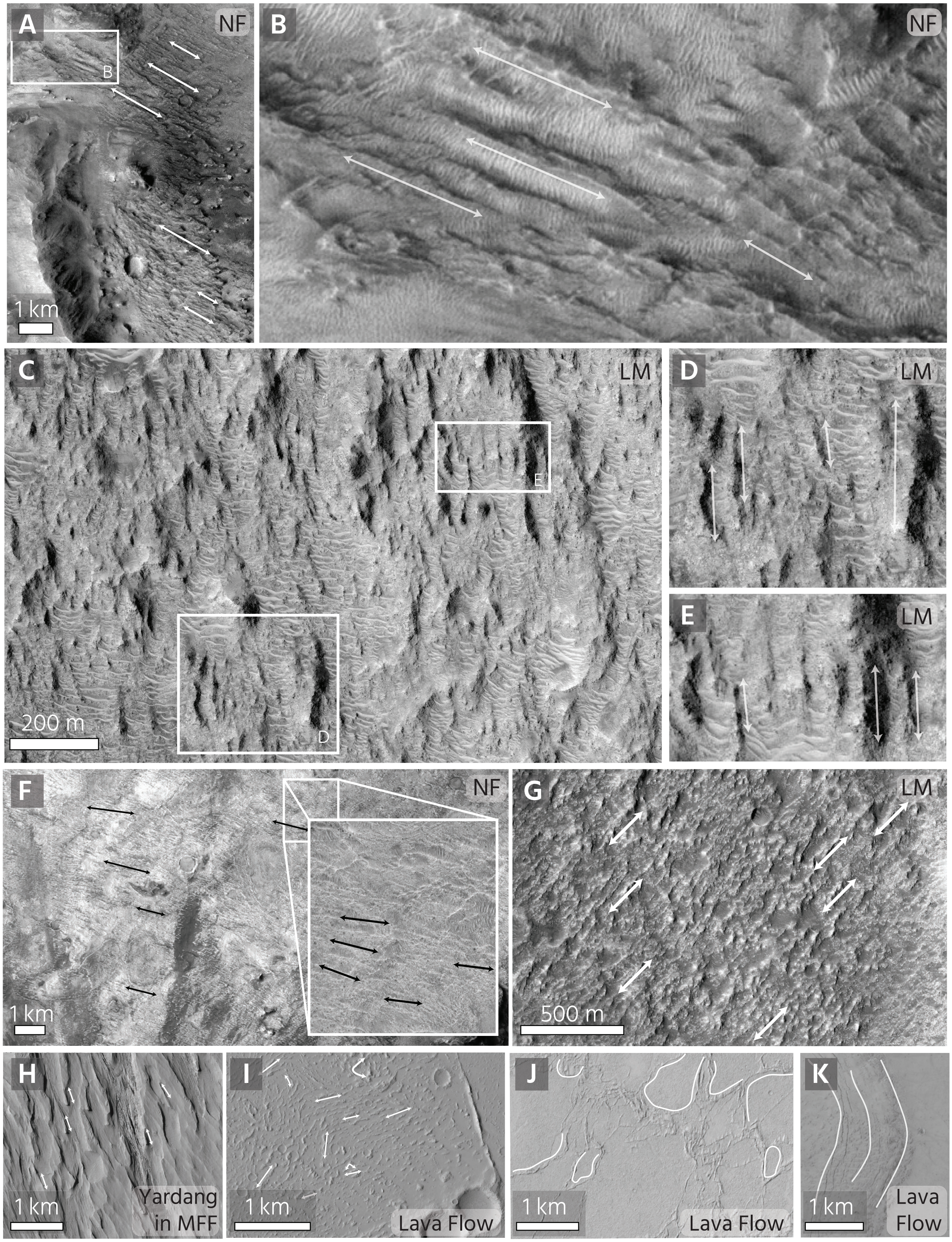

Figure DR8. Putative lava flow features (Hamilton and Christensen, 2005) and other ridge-like morphologies in the olivine-rich unit in the Nili Fossae (NF) and Libya Montes (LM) regions. Yardangs and lava flows observed elsewhere on Mars are shown in the bottom panels. (A,B) Parallel ridges eroded into the olivine-rich unit in Nili Fossae that were previously interepreted as lava flow-related morphologies (Hamilton and Christensen) (CTX image P02_001754_2021_XI_22N281W). (C,D,E) Parallel "ship-hull" shaped ridges in Libya Montes (HiRISE image ESP_016034_1835) identified as yardangs by Bishop et al. (2013). (F) Parallel ridges eroded into the unit in Nili Fossae (CTX image P17_007714_2001_XN_20N281W,) and (G) Libya Montes (HiRISE image PSP_002044_1835). (H) Wind-eroded yardangs in the Medusae Fossae Formation (HiRISE image ESP_017309_1900), which is composed predominantly of fine-grained material. (I) Non-parallel ridges at Daedalia Planum (HiRISE image ESP_028965_1610), (J) platy ridges at Amazonis Planitia (ESP_026381_2060), and (K) concentric ridges in lobate mound at Elysium Planitia (HiRISE image ESP_026461_2080) observed in lava flows. North is up in all images. The morphological characteristics of lava flows on Mars are detailed in Keszthelyi et al. (2000).

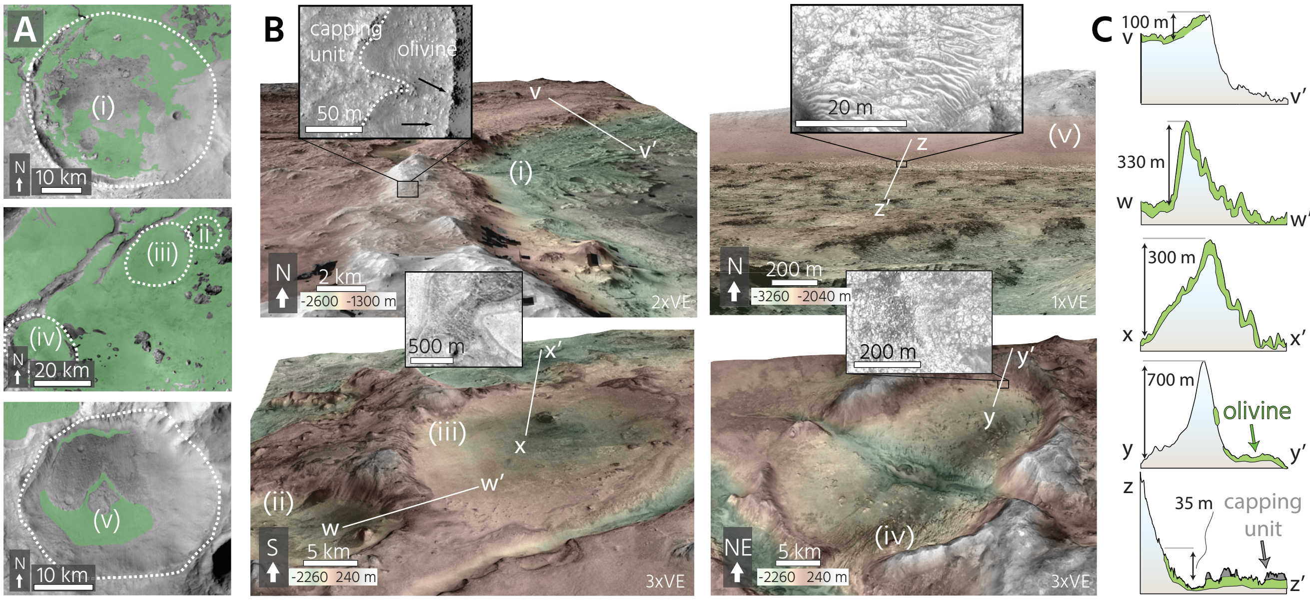

Figure DR9. Draping of crater-rims and similar structures by the olivine-rich unit. Compare with **Figure 3** in the main text. (A) Distribution of olivine-rich unit (green) with respect to craters and crater-like structures, overlain on CTX mosaic base maps (Dickson et al., 2018). The craters and crater-like structures are i) Jezero crater (18.4°N, 77.7°E), ii and iii) two unnamed crater-like structures (22.5°N, 79.1°E; 22.7°N, 79.4°E) in the Nili Fossae region, iv) an unnamed, slightly elongate structure (21.9°N, 78.2°E) interpreted as a crater by Hamilton and Christensen (2005), and v) Hashir crater (3.2°N, 85.0°E). (B) HiRISE imagery draped on CTX topography of craters with rims superposed by the olivine-rich unit. Clockwise from top left: Jezero crater (Nili Fossae) (see **Figure 3**), Hashir crater (Libya Montes), and three unnamed crater-like structures in Nili Fossae. Inset HiRISE imagery of diagnostic polygonal fracturing and banding. Orbital data used, clockwise from top left: HiRISE image PSP_002756_1830 draped over DEM from CTX images D14_032794_1989_XN_18N282W and D15_033216_1989_XN_18N282W (Jezero), HiRISE image PSP_002822_1830 draped over HiRISE DEM DTEEC_002756_1830_002822_1830_A01 (Hashir), CTX image P02_001754_2021_X-I_22N281W draped over H3340_0000 (elongate unnamed crater), and CTX mosaic draped over HRSC DEM H3340_0000 (two unnamed circular craters). (C) Cross section profiles of rim-draping by olivine-rich unit with minimum elevation above surrounding terrain indicated. In CTX imagery, the units also exhibit the characteristic fractured and banded texture of the unit's in-place outcrops recognized by Goudge et al. (2015).

Table DR1. HiRISE Observations Used for Mapping

Nili Fossae
ESP_011630_1985_RED
ESP_011841_2005_RED
ESP_011986_2060_RED
ESP_012039_2010_RED
ESP_012052_2030_RED
ESP_012764_2010_RED
ESP_013041_1975_RED
ESP_013463_1995_RED
ESP_013977_2075_RED
ESP_015942_1980_RED
ESP_016153_2005_RED
ESP_016219_1980_RED
ESP_016364_1980_RED
ESP_016443_1980_RED
ESP_016496_2000_RED
ESP_016509_1980_RED
ESP_016575_1980_RED
ESP_016588_2000_RED
ESP_016720_1980_RED
ESP_016786_1980_RED
ESP_016865_2035_RED
ESP_016931_1980_RED
ESP_017076_1980_RED
ESP_017142_2070_RED
ESP_017221_2015_RED
ESP_017287_1980_RED
ESP_017432_2025_RED
ESP_017498_1980_RED
ESP_017577_2020_RED
ESP_017643_1980_RED
ESP_017788_2000_RED
ESP_017854_1980_RED
ESP_017999_1970_RED
ESP_018065_1975_RED
ESP_018210_1980_RED
ESP_018500_2000_RED
ESP_018566_1980_RED
ESP_018988_1980_RED
ESP_019133_1975_RED
ESP_019476_2005_RED
ESP_019489_2070_RED
ESP_019621_2005_RED
ESP_019845_2000_RED
ESP_020135_2000_RED
ESP_020399_2070_RED
ESP_020755_2025_RED
ESP_021612_1975_RED
ESP_021678_1985_RED
ESP_021757_1975_RED
ESP_021823_2035_RED
ESP_022034_2070_RED
ESP_022456_2030_RED
ESP_022601_1975_RED
ESP_022680_1985_RED
ESP_022746_1985_RED
ESP_022812_2010_RED
ESP_022878_2010_RED
ESP_022957_1985_RED
ESP_023023_1970_RED
ESP_023089_1960_RED
ESP_023102_1985_RED
ESP_023168_1985_RED
ESP_023247_1985_RED
ESP_023379_1985_RED
ESP_023524_1985_RED
ESP_023735_1980_RED
ESP_023814_1970_RED
ESP_024025_2005_RED
ESP_024447_2035_RED
ESP_024513_1980_RED
ESP_024658_1965_RED
ESP_024737_2005_RED
ESP_024882_2060_RED
ESP_025093_2060_RED
ESP_025146_2020_RED
ESP_025370_1980_RED
ESP_025436_1990_RED
ESP_025647_1965_RED
ESP_025713_2070_RED
ESP_025937_1965_RED
ESP_025990_1995_RED
ESP_026003_2055_RED
ESP_026069_1970_RED
ESP_026135_1995_RED
ESP_026280_1975_RED
ESP_026346_2000_RED
ESP_026359_1990_RED
ESP_026425_1985_RED

ESP_026491_2000_RED
ESP_026570_2025_RED
ESP_026636_1975_RED
ESP_026702_1980_RED
ESP_026781_2075_RED
ESP_026992_2025_RED
ESP_027058_1975_RED
ESP_027124_2035_RED
ESP_027269_1970_RED
ESP_027480_2075_RED
ESP_027625_1975_RED
ESP_027691_2025_RED
ESP_027902_1975_RED
ESP_028245_2010_RED
ESP_028390_2010_RED
ESP_028403_2040_RED
ESP_028456_1980_RED
ESP_028535_1990_RED
ESP_028667_2020_RED
ESP_028680_2070_RED
ESP_028746_2010_RED
ESP_028825_2070_RED
ESP_028970_1990_RED
ESP_029023_2075_RED
ESP_029036_1990_RED
ESP_029247_2045_RED
ESP_029946_2020_RED
ESP_030025_1975_RED
ESP_030091_2010_RED
ESP_030170_1985_RED
ESP_030236_1975_RED
ESP_030302_2010_RED
ESP_030869_2010_RED
ESP_030882_2015_RED
ESP_031014_2030_RED
ESP_031225_2050_RED
ESP_031805_1985_RED
ESP_031871_1985_RED
ESP_032016_2015_RED
ESP_032161_2015_RED
ESP_032227_2040_RED
ESP_032372_2020_RED
ESP_032517_2045_RED
ESP_032649_2010_RED
ESP_032662_2020_RED
ESP_032728_2020_RED
ESP_032794_1990_RED
ESP_032873_2020_RED
ESP_032939_2005_RED
ESP_033071_2010_RED
ESP_033084_2020_RED
ESP_033150_1985_RED
ESP_033216_1990_RED
ESP_033295_2020_RED
ESP_033427_2010_RED
ESP_033506_2025_RED
ESP_033572_1995_RED
ESP_033651_1990_RED
ESP_033717_1990_RED
ESP_034007_2020_RED
ESP_034073_1985_RED
ESP_034205_2070_RED
ESP_034284_2020_RED
ESP_034495_1990_RED
ESP_034706_2070_RED
ESP_034772_1980_RED
ESP_034785_2000_RED
ESP_034917_2030_RED
ESP_034996_2030_RED
ESP_035062_1995_RED
ESP_035141_1990_RED
ESP_035352_2025_RED
ESP_035484_2025_RED
ESP_035563_1990_RED
ESP_035629_1990_RED
ESP_035774_2005_RED
ESP_035906_2070_RED
ESP_035919_2005_RED
ESP_035985_1985_RED
ESP_036117_2070_RED
ESP_036328_1985_RED
ESP_036407_1975_RED
ESP_036473_2070_RED
ESP_036552_2000_RED
ESP_036618_1985_RED
ESP_036763_2000_RED
ESP_036829_1980_RED
ESP_036908_2030_RED
ESP_036974_2005_RED
ESP_037040_1980_RED

ESP_037106_2025_RED
ESP_037119_1985_RED
ESP_037185_2010_RED
ESP_037264_1970_RED
ESP_037330_1990_RED
ESP_037396_1985_RED
ESP_037475_2000_RED
ESP_037541_2010_RED
ESP_037607_1990_RED
ESP_037673_2015_RED
ESP_037686_2005_RED
ESP_037739_2015_RED
ESP_037752_1990_RED
ESP_037818_1990_RED
ESP_037963_2040_RED
ESP_038029_1980_RED
ESP_038042_2055_RED
ESP_038240_1990_RED
ESP_038306_1970_RED
ESP_038372_1995_RED
ESP_038385_2020_RED
ESP_038438_1965_RED
ESP_038715_1975_RED
ESP_038781_2035_RED
ESP_038913_2010_RED
ESP_038992_2045_RED
ESP_039124_2015_RED
ESP_039137_2025_RED
ESP_039203_1985_RED
ESP_039269_2010_RED
ESP_039348_1985_RED
ESP_039414_1965_RED
ESP_039480_2015_RED
ESP_039493_2030_RED
ESP_039625_1995_RED
ESP_039770_1965_RED
ESP_039836_1965_RED
ESP_039902_1965_RED
ESP_040047_2015_RED
ESP_040258_2030_RED
ESP_040271_2040_RED
ESP_040825_2025_RED
ESP_040904_1975_RED
ESP_040970_1975_RED
ESP_041115_1975_RED
ESP_041893_1975_RED
ESP_042038_2010_RED
ESP_042249_1975_RED
ESP_042315_1985_RED
ESP_042328_1985_RED
ESP_042394_1990_RED
ESP_042605_1975_RED
ESP_042671_1970_RED
ESP_042750_1970_RED
ESP_042816_2010_RED
ESP_042882_1980_RED
ESP_042961_2010_RED
ESP_043027_2025_RED
ESP_043093_1965_RED
ESP_043106_1990_RED
ESP_043172_1970_RED
ESP_043238_2025_RED
ESP_043528_2020_RED
ESP_043594_1980_RED
ESP_043607_2000_RED
ESP_043673_2020_RED
ESP_043739_1975_RED
ESP_043818_2020_RED
ESP_043884_1975_RED
ESP_043963_2020_RED
ESP_044095_2010_RED
ESP_044161_2005_RED
ESP_044240_2000_RED
ESP_044372_1960_RED
ESP_044385_2000_RED
ESP_044517_1990_RED
ESP_044662_2010_RED
ESP_044794_2010_RED
ESP_044873_1990_RED
ESP_044939_1990_RED
ESP_045005_2010_RED
ESP_045071_2015_RED
ESP_045137_2015_RED
ESP_045216_2045_RED
ESP_045361_2010_RED
ESP_045559_1960_RED
ESP_045572_1990_RED
ESP_045862_2050_RED
ESP_045915_2015_RED
ESP_045928_1985_RED

ESP_045994_1985_RED
ESP_046060_1985_RED
ESP_046126_1970_RED
ESP_046205_2010_RED
ESP_046271_1980_RED
ESP_046350_1985_RED
ESP_046416_2025_RED
ESP_046429_1995_RED
ESP_046640_1955_RED
ESP_046693_2015_RED
ESP_046838_2015_RED
ESP_046851_2040_RED
ESP_046983_1965_RED
ESP_047049_2015_RED
ESP_047128_2045_RED
ESP_047194_1965_RED
ESP_047207_2035_RED
ESP_047339_1980_RED
ESP_047405_2025_RED
ESP_047563_1975_RED
ESP_047774_2020_RED
ESP_047840_2070_RED
ESP_047906_2000_RED
ESP_048051_2015_RED
ESP_048196_1995_RED
ESP_048341_1990_RED
ESP_048473_1965_RED
ESP_048486_1965_RED
ESP_048631_1990_RED
ESP_048697_1970_RED
ESP_048763_2015_RED
ESP_048776_2010_RED
ESP_048842_1985_RED
ESP_048908_1985_RED
ESP_049053_1980_RED
ESP_049119_1980_RED
ESP_049132_2025_RED
ESP_049264_1980_RED
ESP_049330_1980_RED
ESP_049343_1990_RED
ESP_049409_2020_RED
ESP_049475_2015_RED
ESP_049541_1980_RED
ESP_049752_1980_RED
ESP_049818_2005_RED
ESP_049831_1990_RED
ESP_049897_1980_RED
ESP_049963_2005_RED
ESP_050042_1980_RED
ESP_050187_2025_RED
ESP_050253_1980_RED
ESP_050266_2040_RED
ESP_050319_2020_RED
ESP_050385_2020_RED
ESP_050530_2025_RED
ESP_050609_1980_RED
ESP_050675_2020_RED
ESP_050688_2050_RED
ESP_050820_1970_RED
ESP_050899_1985_RED
ESP_050965_2025_RED
ESP_051031_1985_RED
ESP_051097_2010_RED
ESP_051176_2000_RED
ESP_051189_2030_RED
ESP_051321_2005_RED
ESP_051888_1990_RED
ESP_052020_1985_RED
ESP_052165_1975_RED
ESP_052231_1975_RED
ESP_052244_1990_RED
ESP_052389_2005_RED
ESP_052455_1985_RED
ESP_052521_1985_RED
ESP_052798_1965_RED
ESP_052811_1985_RED
ESP_052877_1985_RED
ESP_052943_1985_RED
ESP_052956_2045_RED
ESP_053022_1985_RED
ESP_053088_1980_RED
ESP_053167_1985_RED
ESP_053233_1985_RED
ESP_053246_1990_RED
ESP_053299_1985_RED
ESP_053312_1985_RED
ESP_053378_1985_RED
ESP_053444_1985_RED
PSP_004299_1985_RED
PSP_004444_2000_RED

PSP_004497_2010_RED
PSP_004510_1990_RED
PSP_005354_2015_RED
PSP_005367_2040_RED
PSP_005565_2020_RED
PSP_005644_1965_RED
PSP_005710_2040_RED
PSP_005776_2010_RED
PSP_005855_2020_RED
PSP_005921_2020_RED
PSP_006000_1965_RED
PSP_006211_2045_RED
PSP_006277_2040_RED
PSP_006501_2005_RED
PSP_006633_2010_RED
PSP_006712_2020_RED
PSP_006778_1995_RED
PSP_006791_2050_RED
PSP_006844_2000_RED
PSP_006857_2005_RED
PSP_006923_1995_RED
PSP_006989_2025_RED
PSP_007147_2040_RED
PSP_007200_2005_RED
PSP_007213_2005_RED
PSP_007345_2025_RED
PSP_007358_2015_RED
PSP_007490_2010_RED
PSP_007556_2010_RED
PSP_007569_2020_RED
PSP_007780_1985_RED
PSP_007846_2000_RED
PSP_007925_1990_RED
PSP_008215_2015_RED
PSP_008426_2025_RED
PSP_008571_1995_RED
PSP_008637_2035_RED
PSP_008650_1990_RED
PSP_008716_2015_RED
PSP_008782_2015_RED
PSP_008795_2020_RED
PSP_008861_2000_RED
PSP_008927_2010_RED
PSP_009138_2025_RED
PSP_009217_1975_RED
PSP_009362_2020_RED
PSP_009428_1975_RED
PSP_009494_2010_RED
PSP_009507_2020_RED
PSP_009573_2035_RED
PSP_009639_2010_RED
PSP_009718_2005_RED
PSP_009929_2020_RED
PSP_010074_2020_RED

Libya Montes	
ESP_011709_1840_RED	ESP_027704_1850_RED
ESP_011920_1850_RED	ESP_027770_1850_RED
ESP_011999_1840_RED	ESP_027836_1845_RED
ESP_012289_1840_RED	ESP_028060_1835_RED
ESP_013766_1845_RED	ESP_028548_1825_RED
ESP_015955_1840_RED	ESP_028614_1840_RED
ESP_016034_1835_RED	ESP_028904_1830_RED
ESP_016522_1835_RED	ESP_030328_1840_RED
ESP_016733_1835_RED	ESP_030961_1835_RED
ESP_017089_1835_RED	ESP_031106_1825_RED
ESP_017445_1835_RED	ESP_033453_1845_RED
ESP_017656_1835_RED	ESP_033809_1845_RED
ESP_018223_1830_RED	ESP_034719_1855_RED
ESP_018368_1830_RED	ESP_034864_1825_RED
ESP_019146_1835_RED	ESP_034930_1835_RED
ESP_019357_1835_RED	ESP_035431_1850_RED
ESP_022337_1830_RED	ESP_036064_1850_RED
ESP_022482_1830_RED	ESP_036275_1825_RED
ESP_022548_1830_RED	ESP_036842_1835_RED
ESP_022970_1835_RED	ESP_036921_1845_RED
ESP_023049_1835_RED	ESP_036987_1825_RED
ESP_023392_1825_RED	ESP_037343_1845_RED
ESP_023405_1835_RED	ESP_037488_1845_RED
ESP_023471_1835_RED	ESP_037765_1835_RED
ESP_023682_1830_RED	ESP_038398_1830_RED
ESP_023827_1835_RED	ESP_038530_1830_RED
ESP_024038_1835_RED	ESP_039005_1825_RED
ESP_024460_1835_RED	ESP_039216_1835_RED
ESP_024526_1840_RED	ESP_039849_1835_RED
ESP_024671_1835_RED	ESP_040482_1855_RED
ESP_024961_1835_RED	ESP_041919_1835_RED
ESP_025172_1835_RED	ESP_042064_1835_RED
ESP_025238_1820_RED	ESP_042341_1835_RED
ESP_025515_1825_RED	ESP_042631_1835_RED
ESP_025792_1840_RED	ESP_042763_1835_RED
ESP_025871_1835_RED	ESP_043251_1820_RED
ESP_026082_1845_RED	ESP_043264_1835_RED
ESP_026293_1845_RED	ESP_044319_1825_RED
ESP_026583_1830_RED	ESP_045440_1835_RED
ESP_026649_1835_RED	ESP_045506_1840_RED
ESP_027005_1835_RED	ESP_045941_1820_RED
ESP_027216_1835_RED	ESP_046007_1825_RED
ESP_027427_1835_RED	ESP_046930_1845_RED
ESP_027559_1845_RED	ESP_046996_1840_RED
	ESP_047418_1855_RED

ESP_047853_1835_RED
ESP_048499_1825_RED
ESP_049699_1825_RED
ESP_050411_1835_RED
ESP_050978_1850_RED
ESP_051044_1850_RED
ESP_053668_1835_RED
ESP_053958_1835_RED
PSP_002044_1835_RED
PSP_002756_1830_RED
PSP_002822_1830_RED
PSP_004101_1840_RED
PSP_005512_1840_RED
PSP_005934_1845_RED
PSP_006145_1855_RED
PSP_006514_1835_RED
PSP_006580_1850_RED
PSP_006870_1835_RED
PSP_007015_1835_RED
PSP_007371_1840_RED
PSP_007503_1840_RED
PSP_007582_1840_RED
PSP_007648_1845_RED
PSP_007727_1830_RED
PSP_007938_1850_RED
PSP_008729_1840_RED
PSP_008808_1830_RED
PSP_008874_1845_RED
PSP_010021_1835_RED
PSP_010153_1845_RED
PSP_010364_1835_RED
PSP_010720_1850_RED

Table DR2. CRISM Observations Used for Mapping

Nili Fossae

FRT000028BA_07_IF165L_TRR3	FRT0001642E_07_IF166L_TRR3
FRT00003584_07_IF166L_TRR3	FRT000165F7_07_IF166L_TRR3
FRT00003E12_07_IF166L_TRR3	FRT00016655_07_IF166L_TRR3
FRT00003FB9_07_IF166L_TRR3	FRT00016A73_07_IF166L_TRR3
FRT000047A3_07_IF166L_TRR3	FRT00016F2C_07_IF166L_TRR3
FRT000048B2_07_IF165L_TRR3	FRT00017103_07_IF165L_TRR3
FRT00005850_07_IF167L_TRR3	FRT000174F4_07_IF166L_TRR3
FRT00005C5E_07_IF166L_TRR3	FRT00017736_07_IF166L_TRR3
FRT0000652E_07_IF166L_TRR3	FRT0001792C_07_IF166L_TRR3
FRT000066A4_07_IF166L_TRR3	FRT00017B1B_07_IF166L_TRR3
FRT000067E1_07_IF166L_TRR3	FRT00017D42_07_IF166L_TRR3
FRT0000722C_07_IF165L_TRR3	FRT0001821C_07_IF166L_TRR3
FRT0000821F_07_IF166L_TRR3	FRT00018524_07_IF166L_TRR3
FRT00008389_07_IF166L_TRR3	FRT00018781_07_IF165L_TRR3
FRT0000857F_07_IF166L_TRR3	FRT00018DCA_07_IF166L_TRR3
FRT0000871C_07_IF166L_TRR3	FRT00019538_07_IF166L_TRR3
FRT000093BE_07_IF166L_TRR3	FRT000199C7_07_IF166L_TRR3
FRT000095FE_07_IF166L_TRR3	FRT00019DAA_07_IF165L_TRR3
FRT000097E2_07_IF166L_TRR3	FRT0001C558_07_IF165L_TRR3
FRT000099BB_07_IF166L_TRR3	FRT0001ECBA_07_IF166L_TRR3
FRT00009C6A_07_IF166L_TRR3	FRT0001FB74_07_IF166L_TRR3
FRT00009D96_07_IF166L_TRR3	FRT00020C77_07_IF166L_TRR3
FRT0000A09C_07_IF166L_TRR3	FRT00021DA6_07_IF166L_TRR3
FRT0000A4FC_07_IF166L_TRR3	FRT00023565_07_IF166L_TRR3
FRT0000AA03_07_IF166L_TRR3	FRT00023728_07_IF166L_TRR3
FRT0000B072_07_IF166L_TRR3	FRT00024A87_07_IF165L_TRR3
FRT0000B438_07_IF166L_TRR3	FRT00024C1A_07_IF165L_TRR3
FRT0000B573_07_IF166L_TRR3	FRT000251C0_07_IF165L_TRR3
FRT0000BC1C_07_IF166L_TRR3	
FRT0000BDA8_07_IF165L_TRR3	
FRT0000BEEB_07_IF166L_TRR3	
FRT0000BFD1_07_IF166L_TRR3	
FRT0000C256_07_IF165L_TRR3	
FRT0000C62B_07_IF166L_TRR3	
FRT0000C968_07_IF166L_TRR3	
FRT0000CBE5_07_IF166L_TRR3	
FRT0001182A_07_IF165L_TRR3	
FRT00011D4C_07_IF166L_TRR3	
FRT00012149_07_IF166L_TRR3	
FRT000128D0_07_IF165L_TRR3	
FRT00013D3B_07_IF165L_TRR3	
FRT00013EBC_07_IF166L_TRR3	
FRT000161EF_07_IF167L_TRR3	
FRT0000B472_07_IF165L_TRR3	
FRT0000B4B5_07_IF165L_TRR3	
FRT0000BAC3_07_IF165L_TRR3	
FRT0000BC7D_07_IF165L_TRR3	
FRT0000CE72_07_IF165L_TRR3	
FRT00011C4D_07_IF165L_TRR3	
FRT00012DE6_07_IF165L_TRR3	
FRT0001647D_07_IF165L_TRR3	
FRT0001754F_07_IF165L_TRR3	
FRT00017DB3_07_IF165L_TRR3	

Libya Montes

FRT00003B63_07_IF165L_TRR3
FRT00007F47_07_IF166L_TRR3
FRT000085D7_07_IF165L_TRR3
FRT00008CA3_07_IF165L_TRR3
FRT00009657_07_IF165L_TRR3
FRT00009A01_07_IF165L_TRR3
FRT0000A377_07_IF165L_TRR3
FRT0000A542_07_IF165L_TRR3
FRT0000A819_07_IF165L_TRR3
FRT0000A909_07_IF165L_TRR3
FRT0000B0CB_07_IF165L_TRR3
FRT0000B22B_07_IF165L_TRR3

Table DR3. DEMs and Stereopairs Used for Outcrop Measurements

HiRISE DEMs Used for Outcrop Measurements
(generated by HiRISE team at the University of Arizona)
Nili Fossae
DTEEC_016364_1980_016219_1980_U01
DTEEC_016443_1980_015942_1980_U01
DTEEC_016509_1980_016575_1980_U01
DTEEC_017076_1980_016931_1980_U01
DTEEC_002888_2025_002176_2025_A01
Libya Montes
DTEEC_002756_1830_002822_1830_A01
DTEEC_007727_1830_008808_1830_A01
DTEEC_016034_1835_017089_1835_A01

HiRISE Stereopairs Used to Construct DEMs for this Study
Nili Fossae
ESP_043818_2020_ESP_043963_2020
ESP_027691_2025_ESP_026992_2025
ESP_044095_2010_ESP_044662_2010
ESP_045005_2010_ESP_045361_2010
ESP_053945_1985_ESP_053879_1985
Libya Montes
ESP_026649_1835_ESP_028060_1835
ESP_042763_1835_ESP_043264_1835
ESP_022337_1830_ESP_022482_1830

CTX Stereopairs Used to Construct DEMs for this Study
D02_028047_2037_D03_028192_2037
D14_032794_1989_D15_033216_1989
D17_033849_2002_F23_044794_1996
F02_036618_1985_F04_037396_1985
F04_037185_2019_F04_037541_2019
F05_037607_2008_F05_037752_2008
F19_043264_1863_G22_026649_1835
F21_043818_2020_F21_043963_2020
G13_023405_1840_G15_024038_1835
J01_045005_2010_J01_045361_2010
P03_002044_1836_P20_008874_1822

HRSC DEMs Used for Outcrop Measurements
H0988_0000_DA4
H3340_0000_DA4

Table DR4 Thickness Measurements of Olivine-Rich Unit Outcrops

Outcrop Number	Outcrop Locale	Coordinates	Average Outcrop Thickness (m)	95% Confidence (m)	Distance* (km)	Number of Bands	Thickness of Bands (m)	Complete Section?
1	Northeast Syrtis	77.04, 17.761	15	2	0	-	-	Y
2	Northeast Syrtis	77.05, 17.771	16	1	1	-	-	Y
3	Northeast Syrtis	77.041, 17.774	21	2	1	-	-	Y
4	Northeast Syrtis	77.059, 17.769	17	2	1	-	-	Y
5	Northeast Syrtis	77.03, 17.81	13	1	2	-	-	Y
6	Northeast Syrtis	77.018, 17.818	14	1	2	-	-	Y
7	Northeast Syrtis	77.028, 17.823	16	1	2	-	-	Y
8	Northeast Syrtis	77.049, 17.836	20	1	3	-	-	Y
9	Northeast Syrtis	77.025, 17.856	19	1	4	-	-	Y
10	Northeast Syrtis	77.115, 17.85	13	2	7	-	-	Y
11	Northeast Syrtis	77.091, 17.873	10	1	8	7	1.4	Y
12	Northeast Syrtis	77.113, 17.866	9	2	8	7	1.2	Y
13	Northeast Syrtis	72.085, 17.881	10	2	8	9	1.1	Y
14	Northeast Syrtis	77.099, 17.887	12	1	8	7	1.7	Y
15	Northeast Syrtis	77.106, 17.9	10	1	9	7	1.4	Y
16	Northeast Syrtis	77.113, 17.92	11	2	11	-	-	Y
17	Northeast Syrtis	77.018, 17.977	23	3	11	-	-	Y
18	Northeast Syrtis	77.029, 17.993	19	6	12	-	-	Y
19	Northeast Syrtis	77.305, 17.951	11	2	17	-	-	Y
20	Northeast Syrtis	77.32, 17.959	17	2	18	-	-	Y
21	Northeast Syrtis	77.323, 17.969	12	1	18	-	-	Y
22	Northeast Syrtis	77.321, 17.929	10	1	19	-	-	Y
23	Nili Fossae	76.613, 19.158	14	2	65	-	-	Y
24	Nili Fossae	76.614, 19.173	7	1	67	-	-	Y
25	Nili Fossae	76.596, 19.182	10	2	67	-	-	Y
26	Nili Fossae	76.62, 19.207	13	2	69	-	-	Y
27	Nili Fossae	76.607, 19.211	13	2	69	-	-	Y
28	Northern Nili Fossae	77.223, 19.806	9	1	113	-	-	Y
29	Northern Nili Fossae	77.278, 20.023	9	1	127	-	-	Y
30	Northern Nili Fossae	77.6, 20.037	11	1	127	-	-	Y
31	Northern Nili Fossae	77.291, 20.056	14	2	128	-	-	Y
32	Northern Nili Fossae	77.273, 20.076	13	2	129	-	-	Y
33	Northern Nili Fossae	77.297, 20.098	10	2	131	-	-	Y
34	Northern Nili Fossae	77.322, 20.29	16	3	142	-	-	Y
35	Northern Nili Fossae	77.33, 20.296	15	3	143	-	-	Y
36	Jezero Watershed	77.586, 20.72	11	1	172	-	-	Y
37	Jezero Watershed	77.596, 20.725	14	1	173	-	-	Y
38	Jezero Watershed	77.598, 20.789	12	3	176	-	-	Y
39	Jezero Watershed	77.628, 20.797	11	1	177	-	-	Y
40	Jezero Watershed	77.61, 20.844	11	1	178	-	-	Y
41	Jezero Watershed	77.581, 20.876	-	-	179	-	-	Y
42	Jezero Watershed	77.588, 20.866	-	-	179	-	-	Y
43	Jezero Watershed	77.581, 20.857	8	1	179	-	-	Y
44	Jezero Watershed	77.608, 20.858	6	1	180	14	0.4	Y
45	Jezero Watershed	77.618, 20.863	6	1	181	9	0.6	Y
46	Jezero Watershed	77.619, 20.872	10	1	181	9	1.1	Y
47	Jezero Watershed	77.598, 20.882	9	1	181	10	0.9	Y
48	Jezero Watershed	77.615, 20.885	9	0	181	-	-	Y
49	Northern Nili Fossae	77.094, 21.786	6	1	220	15	0.4	Y
50	Northern Nili Fossae	77.124, 21.899	6	1	227	8	0.8	Y
51	Northern Nili Fossae	77.121, 21.941	4	1	229	13	0.3	Y
52	Northern Nili Fossae	77.166, 21.946	5	2	230	-	-	Y
53	Northern Nili Fossae	77.164, 21.961	3	1	231	-	-	Y

54	Northern Nili Fossae	77.087, 21.989	7	1	231	-	-	Y
55	Northern Nili Fossae	77.19, 22	3	0	233	11	0.2	Y
56	Northern Nili Fossae	77.12, 22.012	6	2	233	11	0.5	Y
57	Northern Nili Fossae	77.095, 22.185	4	1	243	13	0.3	Y
58	Northern Nili Fossae	77.215, 22.217	5	1	246	-	-	Y
59	Northern Nili Fossae	77.245, 22.215	2	1	246	-	-	Y
60	Northern Nili Fossae	77.221, 22.221	6	2	247	-	-	Y
61	Northern Nili Fossae	72.259, 22.231	11	2	248	-	-	Y
62	Northern Nili Fossae	77.228, 22.227	5	1	248	8	0.6	Y
63	Northern Nili Fossae	77.201, 22.268	7	2	250	-	-	Y
64	Northern Nili Fossae	77.186, 22.309	3	1	251	-	-	Y
65	Northern Nili Fossae	77.188, 22.375	9	2	254	-	-	Y
66	Carbonate Plains	78.634, 21.976	5	2	261	25	0.2	Y
67	Carbonate Plains	78.665, 21.969	4	2	262	19	0.2	Y
68	Carbonate Plains	78.654, 21.975	6	2	262	24	0.3	Y
69	Carbonate Plains	78.656, 21.974	8	2	262	13	0.6	Y
70	Northern Nili Fossae	77.275, 23.233	4	3	300	-	-	N
71	Northern Nili Fossae	77.284, 23.338	5	3	307	-	-	N
72	Northern Nili Fossae	77.258, 23.328	8	2	307	-	-	N
73	Northern Nili Fossae	77.201, 23.998	3	0	344	-	-	N
74	Libya Montes West	84.001, 3.5	53	4	0	-	-	N
75	Libya Montes West	83.973, 3.565	24	4	0	-	-	N
76	Libya Montes West	84.028, 3.41	43	3	0	-	-	N
77	Libya Montes West	83.966, 3.484	46	5	13	-	-	N
78	Libya Montes West	83.959, 3.493	31	3	17	-	-	N
79	Libya Montes West	84.004, 3.488	40	4	18	-	-	N
80	Libya Montes West	84.008, 3.566	72	3	19	-	-	N
81	Libya Montes West	83.963, 3.506	32	3	19	-	-	N
82	Libya Montes West	84.082, 3.521	32	5	19	-	-	N
83	Libya Montes West	84.013, 3.57	74	4	20	-	-	N
84	Libya Montes West	83.958, 3.57	30	3	20	-	-	N
85	Libya Montes West	84.071, 3.496	29	4	20	-	-	N
86	Libya Montes West	84.006, 3.553	54	3	21	-	-	N
87	Libya Montes West	84.02, 3.45	87	2	21	-	-	N
88	Libya Montes West	84.025, 3.605	89	7	21	-	-	N
89	Libya Montes West	83.998, 3.583	36	4	25	-	-	N
90	Libya Montes West	84.858, 3.445	54	11	56	-	-	N
91	Libya Montes West	84.781, 3.413	39	4	57	-	-	N
92	Libya Montes West	84.814, 3.469	86	3	58	-	-	N
93	Libya Montes West	84.769, 3.494	104	6	59	-	-	N
94	Libya Montes West	84.877, 3.439	70	6	61	-	-	N
95	Libya Montes	84.957, 3.538	-	-	62	-	-	N
96	Libya Montes	84.958, 3.549	-	-	63	-	-	N
97	Libya Montes	84.97, 3.54	5	2	63	17	0.3	N
98	Libya Montes	84.984, 3.53	10	2	64	12	0.8	N
99	Libya Montes	84.986, 3.525	-	-	64	-	-	N
100	Libya Montes	84.992, 3.528	5	2	64	21	0.2	N
101	Libya Montes	84.993, 2.527	-	-	64	-	-	N
102	Libya Montes	84.993, 3.496	4	1	65	8	0.5	N
103	Hashir	84.989, 3.183	-	-	65	-	-	Y
104	Hashir	84.976, 3.192	68	14	65	-	-	Y
105	Hashir	84.993, 3.189	-	-	65	-	-	Y
106	Libya Montes	85.006, 3.494	14	1	67	9	1.6	N
107	Libya Montes	85.009, 3.497	14	1	67	7	2.0	N
108	Hashir	84.998, 3.196	-	-	65	-	-	Y
109	Libya Montes	85.026, 3.486	8	2	67	11	0.7	N
110	Libya Montes	85.031, 3.485	2	2	67	8	0.3	N

111	Libya Montes	85.033, 3.486	5	2	68	12	0.4	N
112	Libya Montes	85.046, 3.556	11	1	68	-	-	N
113	Libya Montes	85.048, 2.567	6	3	69	18.0	0.3	N
114	Libya Montes	85.062, 3.566	12	2	69	15.0	0.8	N
115	Libya Montes	85.06, 3.562	7	1	69	10.0	0.7	N
116	Libya Montes	85.058, 3.531	25	1	69	28.0	0.9	N
117	Libya Montes	85.065, 3.564	14	1	69	12.0	1.1	N
118	Libya Montes East	86.054, 3.372	31	7	125	-	-	N
119	Libya Montes East	86.054, 3.395	32	7	127	-	-	N
120	Libya Montes East	86.097, 3.4	14	5	130	-	-	N
121	Libya Montes East	86.105, 3.403	22	7	132	-	-	N
122	Libya Montes	84.963, 3.539	-	-	64	-	-	N
123	Libya Montes	84.986, 3.526	-	-	65	-	-	N
124	Libya Montes	85.005, 3.4	48	6	66	-	-	Y

*Distance along x-x' (Nili Fossae) or y-y' (Libya Montes) lines. See Figures 1B,C and 4

Table DR5. Outcrop Orientation Measurements[1]

Outcrop			Cap Unit		Basement		Band 1		Band 2		Band 3		Band 4		Band 5		Band 6		Band 7		Band 8		Band 9	
Number	Outcrop Locale	Coordinates	Dip (°)	Error[2]	Dip (°)	Error	Dip (°)	Error	Dip (°)	Error	Dip (°)	Error	Dip (°)	Error	Dip (°)	Error	Dip (°)	Error	Dip (°)	Error	Dip (°)	Error	Dip (°)	Error
1	Northeast Syrtis	77.04, 17.761	1	1	1	1																		
2	Northeast Syrtis	77.05, 17.771	1	2	0	1																		
3	Northeast Syrtis	77.041, 17.774	2	1	0	1																		
4	Northeast Syrtis	77.059, 17.769	1	1	3	2	3	1	1	1														
6	Northeast Syrtis	77.018, 17.818	1	2	0	1	1	1																
7	Northeast Syrtis	77.028, 17.823	0	1	0	1																		
8	Northeast Syrtis	77.049, 17.836	4	1	0	1																		
10	Northeast Syrtis	77.115, 17.85	1	2	0	1	0	1	0	1	1	1												
11	Northeast Syrtis	77.091, 17.873	0	1	1	1	0	1	1	1	1	2	1	2	0	1	0	2	1	1				
13	Northeast Syrtis	72.085, 17.881	2	1	0	1	0	1	0	1	0	1												
14	Northeast Syrtis	77.099, 17.887	2	0	0	2	1	1	0	2	1	1	0	1	0	1								
15	Northeast Syrtis	77.106, 17.9	2	1	1	1	1	1	1	1														
19	Northeast Syrtis	77.305, 17.951	0	1	0	1																		
20	Northeast Syrtis	77.32, 17.959	0	1	0	1																		
21	Northeast Syrtis	77.323, 17.969	1	2	0	2																		
36	Jezero Watershed	77.586, 20.72	1	1	2	1																		
37	Jezero Watershed	77.596, 20.725	1	1	2	1																		
38	Jezero Watershed	77.598, 20.789	2	1	2	1																		
39	Jezero Watershed	77.628, 20.797	3	1	1	1																		
40	Jezero Watershed	77.61, 20.844	3	0	0	1																		
41	Jezero Watershed	77.581, 20.876	2	1	2	1	2	1	2	1	2	1												
42	Jezero Watershed	77.588, 20.866	1	1			1	1	1	0	1	1	1	1	1	1	1	-						
43	Jezero Watershed	77.581, 20.857	1	1			0	1	1	1	1	1	1	1										
44	Jezero Watershed	77.608, 20.858	3	0	2	1	2	1	2	1	2	0	1	1										
45	Jezero Watershed	77.618, 20.863	1	1			1	0	1	1	1	1												
47	Jezero Watershed	77.598, 20.882	1	1	3	1	2	1	2	1	2	1												
48	Jezero Watershed	77.615, 20.885	1	1	4	1	2	1	1	1	2	1												
60	Northern Nili Fossae	77.221, 22.221	2	1	1	1																		
63	Northern Nili Fossae	77.201, 22.268	5	1	4	1	5	2	4	1														
95	Libya Montes	84.957, 3.538			7	2	8	0	7	1	6	2												
96	Libya Montes	84.958, 3.549			8	1	7	2	6	1														
99	Libya Montes	84.986, 3.525			8	1	16	2	16	2	16	2	10	1	15	3								
101	Libya Montes	84.993, 3.527			12	0	5	2	10	0	11	1	11	1	11	1								
103	Libya Montes (Hashir)	84.989, 3.183	11	2	12	1	8	3	14	2														
105	Libya Montes (Hashir)	84.993, 3.189	6	3	10	2	8	1	14	1	18	3												
108	Libya Montes (Hashir)	84.998, 3.196	11	3	15	2	16	1	11	1														
126	Libya Montes	85.006, 3.451			9	1	9	1	9	1	13	3	13	4	14	2	12	3						
127	Libya Montes	85.013, 3.424			10	1	2	1	7	1	7	1	7	1	7	2	4	2	5	2	11	1	1	1
112	Libya Montes	85.046, 3.556			11	1	8	0	10	0	13	0	13	0										
113	Libya Montes	85.048, 3.567			5	4	11	1	8	2	4	1	2	1	2	1	2	2	3	2	3	2		
122	Libya Montes	84.963, 3.539			10	1	12	1	10	1														
123	Libya Montes	84.986, 3.526			10	2	12	2	10	1														
124	Libya Montes	84.958, 3.54			4	1	6	3	6	1														
125	Libya Montes	84.963, 3.556			15	3	15	3	8	3	8	3	8	3	7	1	7	1	5	4				

[1]Measured on HiRISE DEMs
[2]Errors reported to the 95% confidence interval

Table DR 6. Hypothesis table for possible emplacement mechanisms of the olivine-rich unit

	Syrtis-Isidis Region Ash	Other Ash	Aeolian Erg	Lava Flow	Isidis Melt Sheet	Isidis Condensate	Other Impact Product
Observed/Measured Features							
Drapes Topography	✓	✓	x	?	x	?	?
Flow Features Absent	✓	✓	✓	?	?	?	?
Superposes Crater Rims Generally	✓	✓	✓	x	✓	?	?
Superposes Post-Isidis Crater Rims	✓	✓	✓	x	x	x	?
Original Thickness Regionally Variable up to 10^2 m	✓	✓	✓	✓	✓	?	?
$Fo_{68\text{-}91}$ Olivine 10-30%	✓	✓	?	✓	✓	✓	✓
Readily Deflated/Moderate Thermal Inertia Values	✓	✓	✓	x	x	?	?
Poorly Crater-Retaining	✓	✓	✓	x	x	?	?
Yardangs	✓	✓	✓	x	x	?	?
Olivine Crystals ~1 mm	✓	x	x	✓	✓	x	x
Layered Deposits	✓	✓	✓	✓	?	?	?
Layers <1 m	✓	✓	✓	x	x	x	x
Many Thin Layers of Alternating Tonality	✓	✓	?	x	x	x	x
Cross-Bedding Not Observed	✓	✓	?	✓	✓	✓	✓
Homogeneous Comp. Across ~10^5 km^2	✓	✓	?	✓	✓	✓	✓
No similar deposits observed outside region	✓	✓	✓	✓	✓	x	x